2017

High dynamic range display systems

Ruidong Zhu
University of Central Florida

HIGH DYNAMIC RANGE DISPLAY SYSTEMS

by

RUIDONG ZHU
B.S. HARBIN INSTITUTE OF TECHNOLOGY, 2012

A dissertation submitted in partial fulfillment of the requirements
for the degree of Doctor of Philosophy
in the College of Optics and Photonics
at the University of Central Florida
Orlando, Florida

Fall Term
2017

Major Professor: Shin-Tson Wu

ABSTRACT

High contrast ratio (CR) enables a display system to faithfully reproduce the real objects. However, achieving high contrast, especially high ambient contrast (ACR), is a challenging task. In this dissertation, two display systems with high CR are discussed: high ACR augmented reality (AR) display and high dynamic range (HDR) display. For an AR display, we improved its ACR by incorporating a tunable transmittance liquid crystal (LC) film. The film has high tunable transmittance range, fast response time, and is fail-safe. To reduce the weight and size of a display system, we proposed a functional reflective polarizer, which can also help people with color vision deficiency. As for the HDR display, we improved all three aspects of the hardware requirements: contrast ratio, color gamut and bit-depth. By stacking two liquid crystal display (LCD) panels together, we have achieved CR over one million to one, 14-bit depth with 5V operation voltage, and pixel-by-pixel local dimming. To widen color gamut, both photoluminescent and electroluminescent quantum dots (QDs) have been investigated. Our analysis shows that with QD approach, it is possible to achieve over 90% of the Rec. 2020 color gamut for a HDR display. Another goal of an HDR display is to achieve the 12-bit perceptual quantizer (PQ) curve covering from 0 to 10,000 nits. Our experimental results indicate that this is difficult with a single LCD panel because of the sluggish response time. To overcome this challenge, we proposed a method to drive the light emitting diode (LED) backlight and the LCD panel simultaneously. Besides relatively fast response time, this approach can also mitigate the imaging noise. Finally yet importantly, we improved the display pipeline by using a HDR gamut mapping approach to display HDR contents adaptively based on display specifications. A psychophysical experiment was conducted to determine the display requirements.

To my beloved parents and friends.

ACKNOWLEDGMENTS

First and foremost, I would like to thank Prof. Shin-Tson Wu and his wife Cho-Yan Hiseh, both of whom have supported me mentally and spiritually. Prof. Wu is a visionary leader of our group and his guidance and suggestions helped me a lot during my Ph.D. years. Besides, he is always encouraging us to try out new ideas and explore new research frontiers. Whenever we need guidance, either academically or mentally, Prof. Wu will be there to help us out. I feel so blessed to be in the LCD family. In addition, I can never forget the delicious radish omelet Shinmu cooked for us!

I would also like to thank my committee members: Prof. M. G. Moharam, Prof. Patrick L. LiKamWa and Prof. Jiyu Fang. Thank you for taking your time revising my thesis and helping me with my society awards and scholarship applications.

Working in the LCD group feels like living in an adventurous family: there are always so many wonders to explore with my family members! During my journey, quite a few people helped me for my research adventure. Here I would like to thank Dr. Su Xu, Dr. Jie Sun, Dr. Yuan Chen, Dr. Jin Yan, Dr. Yifan Liu, Dr. Sihui He, Dr. Zhenyue Luo, Dr. Qi Hong, Dr. Daming Xu, Dr. Fenglin Peng, Yun-Han Lee, Haiwei Chen, Guanjun Tan, Juan He, Fangwang Gou, and Yuge Huang. Without your help, I will never achieve what I have done today.

Besides my group members, I am also grateful to my other friends in both the academic world and the industry. I would like to thank Prof. Jiun-Haw Lee from National Taiwan University, who gave us a lot of advices and insightful information about OLED displays. I would also like to thank Mr. Tim Large, Dr. Neil Emerton and Dr. Abhijit Sakar at Microsoft for giving me a fun and challenging research experience.

Finally yet importantly, I would like to express my deepest gratitude to my parents for their unconditional support, both mentally and financially during my Ph.D. years. Thank you for respecting my choices and without your help life here would be much more challenging.

TABLE OF CONTENTS

LIST OF FIGURES

LIST OF TABLES

CHAPTER ONE: INTRODUCTION

We live in a world with extremely high dynamic range (HDR): from direct sunlight to star light the luminance can vary from 10^9 to 10^{-6} cd/m^2 [1-3], which indicates a 15 orders of magnitude of dynamic range. To faithfully reproduce the real world, the display systems also need to have high contrast. Among the many display systems, contrast plays a vital role for augmented reality (AR) systems and HDR displays. Enormous resources have been put into improving the contrast ratio for AR and HDR systems.

1.1. High ambient contrast augmented reality systems

Augmented reality systems are regarded as "the next big thing" for the display industry as they perfectly combine the real world with the virtual world. To achieve this goal, there are two mainstream AR systems: video see-through augmented reality and optical see-through augmented reality. For the former case, the system overlays real world video with computer generated (CG) images, while for the latter the system optically combines real-world view with CG images [4, 5]. While the former approach comes with simpler optical configurations, it is challenging to realize real-time integration because of the image processing and synchronization [6]. As for the latter approach, quite a few optical structures have been proposed to combine the real world with the virtual images [7-9]. Among them, polarizing beam splitter (PBS) is a popular optical component as it can effectively manage the polarization of the display [10]. However, the PBS makes the whole system bulky and heavy, at the same time, PBS alone cannot offer high contrast ratio under strong ambient light.

In this dissertation, we report a compact and high ambient contrast (ACR) AR system [11] by combining a tunable liquid crystal (LC) film with a reflective polarizer [11-13]. When

combined with an ambient light sensor, the tunable LC film works as a smart dimmer to control the ambient contrast ratio whereas the reflective polarizer works similarly to a PBS. The advantages of the tunable LC film are threefold: large tunable range, fast response time and low driving voltage. In terms of the reflective polarizer, it outperforms the PBS because of its compactness and lightweight. Moreover, the design of the reflective polarizer is quite flexible and it is possible to design a functional reflective polarizer to help those people with color vision deficiency (CVD) [14, 15]. The details of the AR systems and the design approach of the functional reflective polarizer will be discussed later in Chapter Two.

1.2. High dynamic range displays

As mentioned before, the dynamic range of the real world is as large as 15 orders of magnitude. However, for a natural scene the contrast ratio is usually 10^5:1 [3, 16]. While contemporary cameras [2] have no problem capturing such a high dynamic range, contemporary standard dynamic range (SDR) displays can only cover a dynamic range of 10^3:1. This is when HDR comes into play. Besides this, another reason that HDR display is superior to SDR display is because of the color appearance phenomena [17], for example, the Hunt effect and Stevens effect, HDR displays with higher peak brightness can offer more vivid colors, thus improving the viewing experience.

Currently, there are two approaches to achieve HDR displays [18, 19]. The first one is organic light emitting diode (OLED) display, which can achieve perfect black level by completely turning off the pixels. The second approach is local dimming liquid crystal display (LCD), where a tunable LED array is used as backlight to achieve deep black levels and high peak brightness.

Even with these technologies, there are three challenges from the hardware side, as described in the following.

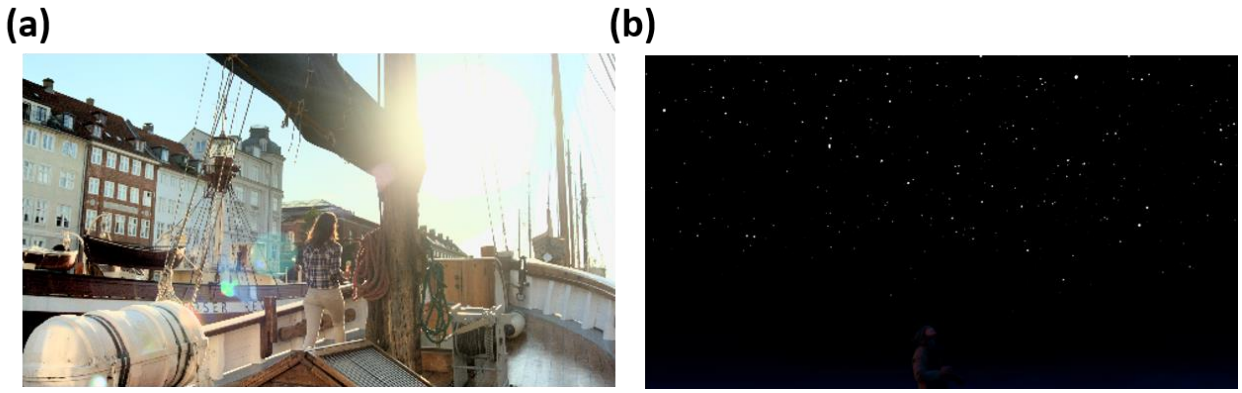

Figure 1: Tone-mapped versions of (a) an HDR scene with luminance of ~1000 nits for the sun area and (b) an HDR frame with luminance of 0 nits for the dark sky.

The first challenge involves the luminance and contrast, as depicted in Figure 1. The images shown here are tone mapped versions [20] of the original HDR frames via highlight compression. For Figure 1 (a), the sun area has a luminance of ~1,000 nits while contemporary SDR display usually has a peak brightness of ~400 nits. The other example is shown in Figure 1 (b), the sky is intended to be pitch black (zero nits), while contemporary SDR display with LC technology typically has a dark state of ~0.25 nits. Most of the time the peak luminance of the HDR content are mastered to ~1,000 nits to cater to contemporary HDR TVs, however, the luminance range problem occurs even for HDR displays as sometimes natural HDR scenes can go way beyond 10,000 nits. All of these indicate we should improve the luminance range and contrast ratio of the displays for representing the real world. From the software viewpoint, the solution to this problem is the tone mapping approach [21] by compressing the luminance and contrast range of the contents to that of the display. From a hardware point of view, the most convenient approach is to use dual panel to improve the contrast ratio [22] , which will be explained later in Chapter

Three. Throughout this dissertation, if not specified otherwise, the HDR contents are from the HDR clip *Colors of the Journey*.

The second problem is about the color gamut. Professional HDR contents are encoded with BT.2020 color gamut [23-25] while most of contemporary SDR displays can only fulfill sRGB. This is simulated in Figure 2, where the image on the right side is not color managed. It is clear that Figure 2 (b) is less saturated than the original content in Figure 2 (a). The problem can be partially mitigated by color gamut mapping [26-28] which transforms all the colors to stay within the device color gamut. The ultimate way to solve the problem of color gamut is to build up a display with Rec. 2020 color gamut. Among the technologies to achieve the goal, quantum dot (QD) technology is a viable candidate, which will be described in detail later in Chapter Four.

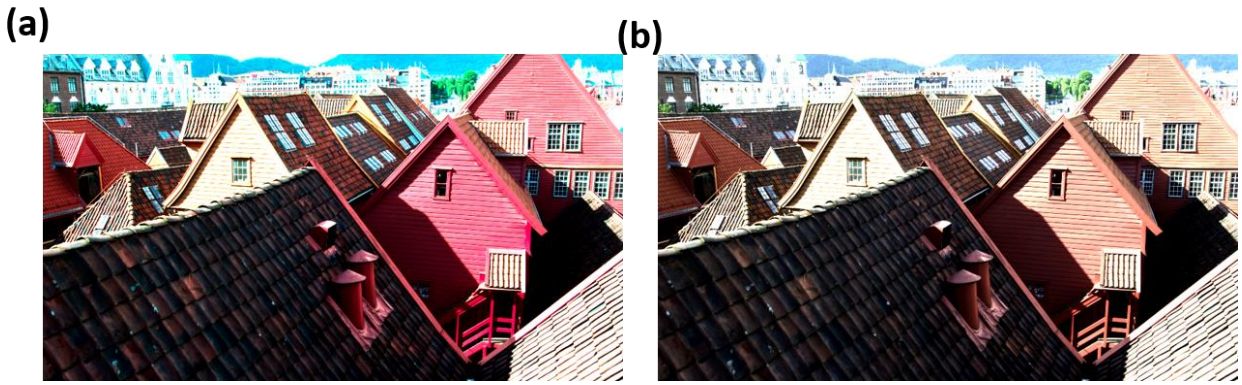

Figure 2: How color gamut affects the performance of a display: (a) the original contents are encoded with BT. 2020 and (b) displaying the content on a sRGB display without gamut mapping (simulated images)

Moreover, the final difficulty is about the bit-depth, as contemporary 8-bit gamma encoding might result in visible banding because of quantization errors within the extended luminance range. This effect is simulated in Figure 3. From Figure 3 (b) it is obvious that when there is not enough bits, the banding effect is very severe compared to the original content in Figure

3 (a). Currently the display industry is using the dithering process [29], which deliberately adds noise to the image to mitigate the banding effect and improve image quality. However, from Figure 3 (c) it is illustrated that the color banding cannot be fully suppressed. That is why the industry is moving towards a 10-bit solution. Going even a step further, a legitimate goal will be to build a 12-bit display based on the perceptual quantizer (PQ) curve [30], also known as the ST. 2084 standard that covers from 0 to 10,000 nits. In Chapter Five, we will present our scheme to achieve the 12-bit PQ curve based on a local dimming LCD system.

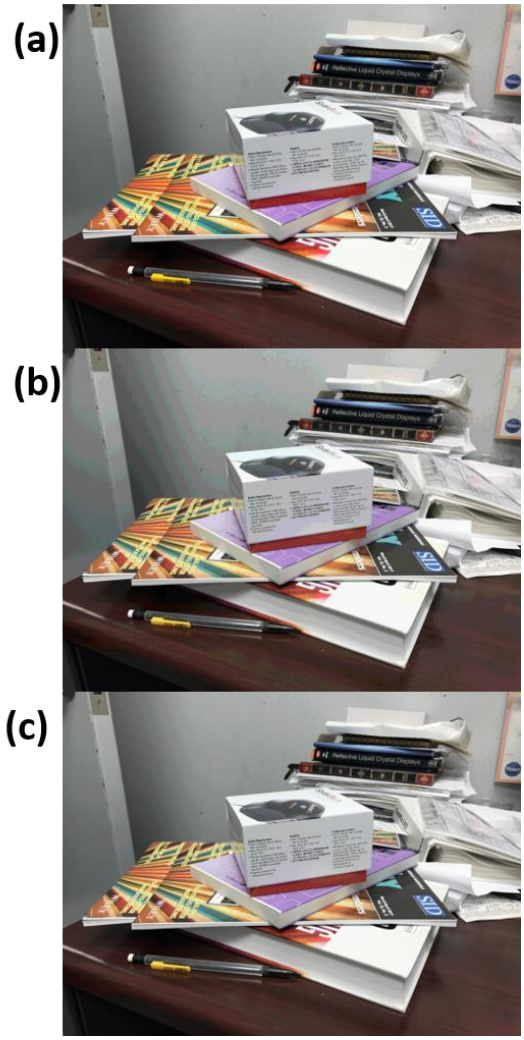

Figure 3: How bit-depth affects the performance of display: (a) the original content with 24 bits in total, (b) displaying the content on a display that only supports 256 colors, and (c) the dithering process to mitigate the banding effect. (Simulated images)

Besides the hardware limitations, another problem is that the current display processing pipeline treats HDR content the same way as it treats the SDR content. After decoding to linear RGB, contemporary display processing pipeline transforms from linear RGB to XYZ through Equation (1):

$$\begin{bmatrix} X \\ Y \\ Z \end{bmatrix} = LM \begin{bmatrix} R \\ G \\ B \end{bmatrix}. \tag{1}$$

Here L is the luminance factor based on the display brightness and M is the color transformation matrix that can be retrieved from the display profile. For a sRGB display:

$$M = \begin{bmatrix} 0.412424 & 0.357579 & 0.180464 \\ 0.212656 & 0.715158 & 0.0721856 \\ 0.0193324 & 0.119193 & 0.950444 \end{bmatrix}. \tag{2}$$

With this approach, RGB values smaller than or equal to unity are transformed as is, while RGB values larger than unity are clipped to one. In this way, a RGB value of (1,1,1) is transformed to display white.

While this pipeline works well with SDR content, for HDR content it can distort the creator's intention, as demonstrated in Figure 4 (a). This image is a frame from the HDR trailer of *Life of Pi*. Much of the scene is interpreted as white and it appears that the actor is travelling under direct sunlight. However, as demonstrated in Figure 4 (b), which is a tone-mapped version of the original scene via highlight compression, the real intention of the creator is that the actor is actually

travelling at sunset or sunrise. In this sense, the contemporary approach in displaying HDR content could incorrectly render the creator's intention.

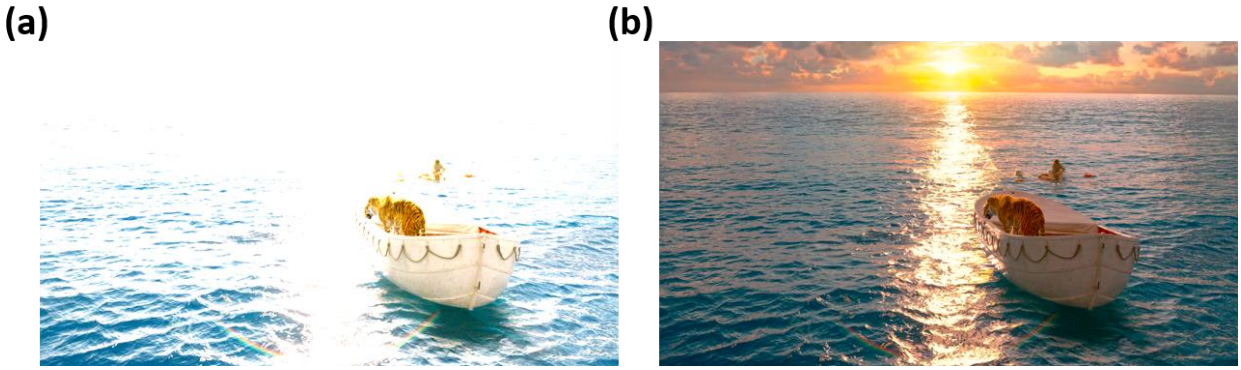

Figure 4: (a) How HDR content are currently displayed on SDR devices, and (b) the real intention of the creator (tone mapped version of the original image)

The reason that contemporary display principle does not work is that for HDR content, the linear RGB values can go beyond unity. For example, for Figure 4 , this clip has a luminance factor L of 80 and reference white is 80 nits. In this way, the grayish clouds area (with RGB values around 2) is actually ~160 nits while contemporary display "interpret" that they are beyond display peak brightness and clipped them to display white.

To solve this problem, we propose a new HDR gamut mapping approach to display HDR contents adaptively based on the display specifications, this part will be discussed in Chapter Six.

CHAPTER TWO: HIGH AMBIENT CONTRAST AUGMENTED REALITY SYSTEMS

The device configuration of Google Glass, a typical AR system is shown in Figure 5. It consists of a display system, a collimating lens system, and a PBS. The PBS partially reflects the display light and transmits the ambient light. It is obvious from the schematic view that the PBS makes the whole system bulky.

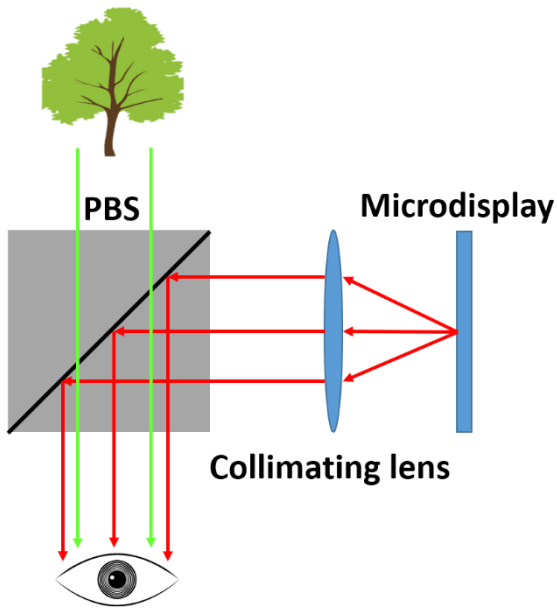

Figure 5: Working principle of Google Glass

Besides system compactness, another problem associated with the PBS is its ambient contrast ratio (ACR). The following equation [11] can be used to determine how much light can be transmitted by the PBS:

$$L_i = \int t_i(\lambda) I_i(\lambda) d\lambda. \tag{3}$$

Here $i=x,y$ represents the x and y polarization, respectively, $t(\lambda)$ is the wavelength dependent transmittance and $I(\lambda)$ is light spectral power distribution (SPD). Most of the time the ambient light is unpolarized, thus Equation (3) can be simplified as:

$$L_a = \frac{1}{2}\int [t_x(\lambda) + t_y(\lambda)] I(\lambda) d\lambda. \tag{4}$$

Here *a* stands for ambient light. Similarly, the total reflected display light is:

$$L_D = \int [r_x(\lambda) I_{Dx}(\lambda) + r_y(\lambda) I_{Dy}(\lambda)] d\lambda. \tag{5}$$

Again r_x=1-t_x and r_y=1-t_y is the wavelength dependent reflectance of the PBS, respectively and *D* stands for the displayed light. For simplicity, we will assume *I* is constant across the wavelength and *r*=*t*=0.5. In this way for OLED display where the display light is unpolarized [31] and LCD where the display light is linearly polarized, the ACR can be written as:

$$ACR = \frac{L_{Don} + L_a}{L_{Doff} + L_a} = \frac{I_{Don} + I_a}{I_{Doff} + I_a}. \tag{6}$$

Here *on* and *off* means the on and off states of the display. For an ideal AR system, we want the display light and the ambient light to fuse together, thus making the viewing experience immersive. For this purpose, I_{Don} should be close to I_a. A typical outdoor display today has a peak luminance of ~2000 nits whereas in broad daylight the luminance of the ambient light can easily go over 20000 nits. Such high luminance will deteriorate the display image.

From Equation (6), it is quite straightforward that there are two ways to improve the ACR: improving the display brightness or attenuating the ambient light. Because of power consumption and lifetime [19] concerns, further improve the display brightness to beyond 20000 nits is not feasible. Thus leaving us to the only solution of attenuating the ambient light level. This is exactly the concept we utilized in our AR system.

2.1 A high ambient contrast augmented reality system

The device configuration of our AR system is shown in Figure 6: the tunable transmittance LC film is laminated on the front surface of the eyeglasses and the reflective polarizer/functional reflective polarizer is laminated on the back surface of the eyeglass. For the polarized display, a possible choice is a liquid crystal on silicon (LCOS) [32-34] pico-projector with an output angle range of ±15°.

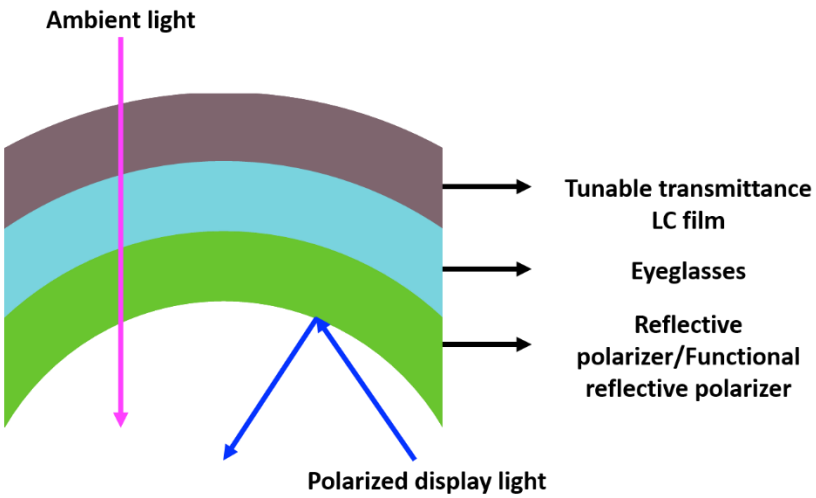

Figure 6: Device configuration of our high ambient contrast system.

The tunable-transmittance LC film is tuned electronically and pairs together with an ambient light sensor so that the LC film is clear at low lux level and it turns to a dark state at high ambient light conditions, thus ensuring a high ACR under all conditions. Because of this we call the film as a smart dimmer. The performance of the tunable transmittance LC film will be discussed later in this chapter. The reflective polarizer, also known as dual brightness enhancement film (DBEF) [11-13], works the same way as the PBS by reflecting one polarization while transmitting the other. The main advantages of the reflective polarizer are twofold: its size can be much larger and its weight much lighter than those of

PBS. Moreover, if we replace the reflective polarizer with our specially designed functional reflective polarizer, such system can help people with CVD, more precisely people with anomalous trichromacy [35, 36]. The design and performance of the functional reflective polarizer will also be demonstrated later. Besides AR systems, our device can also be laminated to the windshield for high ACR vehicular displays.

2.2 The tunable transmittance LC film

A tunable transmittance system is desirable for applications where the ambient light is strong, for example, outdoor displays, energy efficient smart windows and car windshields. Several approaches have been developed to achieve tunable transmittance. Among these approaches, the most mature and commercially successful approach is the photochromic materials. [37] used in transition glasses. However, besides their exceptional performance, transition glasses often suffer from sluggish response time, as measured in Figure 7. In our experiment, we irradiated UV light onto a commercial transition glass and measured its time-dependent transmittance. As Figure 7 (a) depicts, the transmittance drops from ~83% to ~10% in 30s. As soon as the UV lamp was turned off, the transmittance changes back to ~83% gradually in 25 min [Figure 7 (b)]. While for the eye response, the pupil regulates the amount of light entering the eye cavity by changing its diameter, taking between 2-5 s to complete the process [38]. The retina on the other hand needs within 1-2 min to adapt completely to the new lighting state through activation and deactivation of photoreceptor cells [38]. It is clear that the transition glass is not as fast as the human visual system. Such a slow response time is not practical for AR systems and thus we proposed a fast-response tunable transmittance LC film.

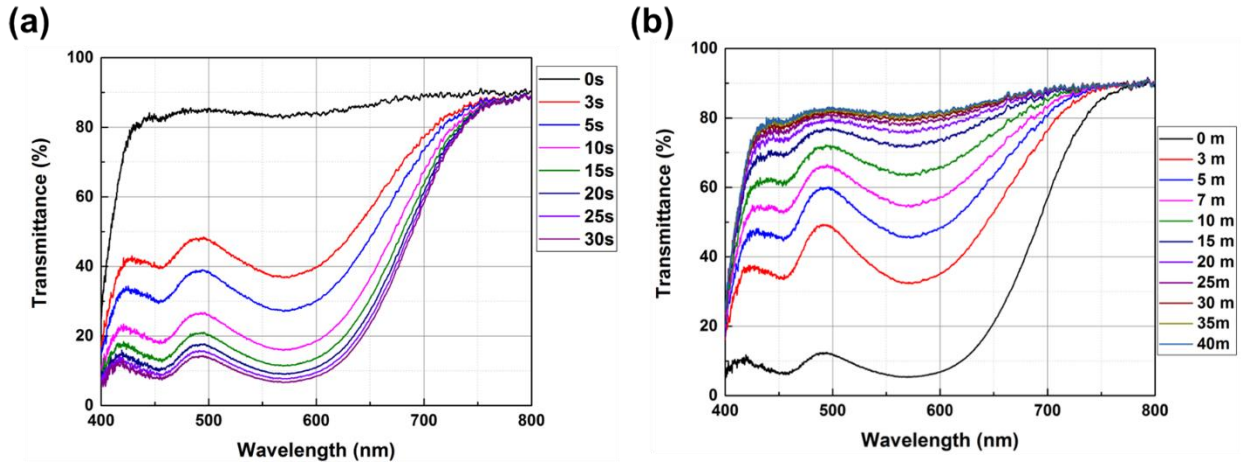

Figure 7: Time-dependent transmittance of a commercial transition glass: (a) from bright state to dark state and (b) from dark state to bright state.

Our voltage-driven tunable transmittance LC film is powered by AlphaMicron's e-Tint technology based on the guest-host approach [39]. In this approach, the LC host ($\Delta\varepsilon<0$) is doped with ~3% black dichroic dyes and a small amount of chiral agent. The working principle of the guest-host LC cell is illustrated in Figure 8. The LC directors are in pink and the dichroic dyes are in black. At zero volt, the LC directors and dichroic dyes are homeotropically aligned and the absorption loss of the incident white light is minimal. Thus, the LC cell is highly transparent. Once the voltage exceeds a threshold, the LC directors and dichroic dyes are reoriented by the electric field to form a 180° super twisted nematic (STN) mode [40] because of the doped chiral agent Such a 180° STN guest-host structure absorbs the incident light strongly and the effect is insensitive to the polarization of the incident white light. The detailed mechanisms of such a chiral-homeotropic cell (without dyes) has been described in [40].

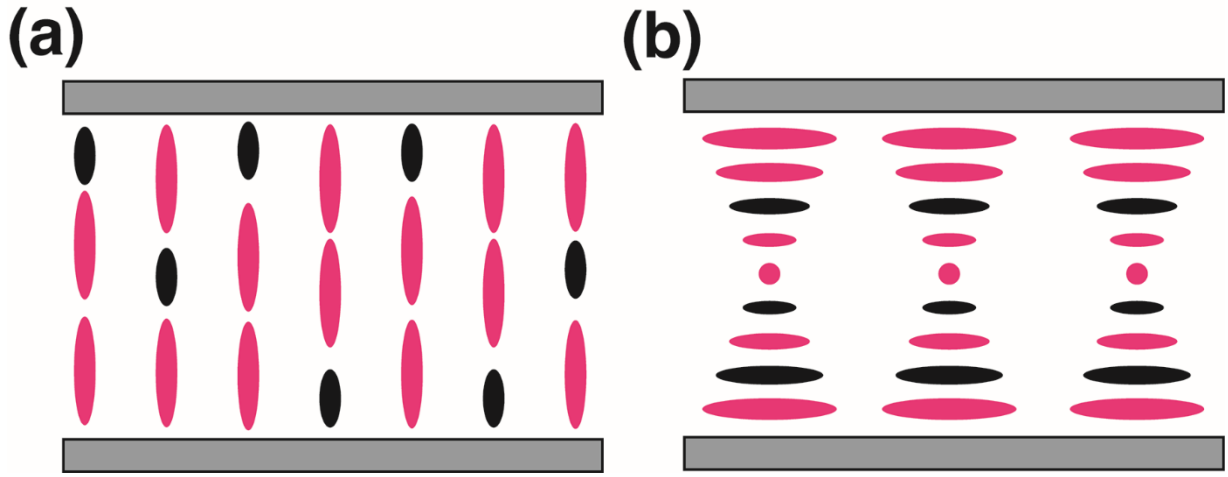

Figure 8: Working principle of the tunable transmittance LC film at (a) bright state and (b) dark state.

The voltage-dependent transmittance of our LC cell is shown in Figure 9: from the bright state (V=0) to the dark state (8V), the transmittance varies from ~73% to ~26%. With an embedded ambient light sensor, the LC film can control the transmittance adaptively according to its brightness. As a result, it helps to obtain high ACR. Besides the tunable transmittance, the measured turn-on time (bright to dark) is 3.8 ms and turn-off time (dark to bright) is 50.5 ms. Such response time is at least 10X faster than that of transition glasses and is sufficient for eyewear applications.

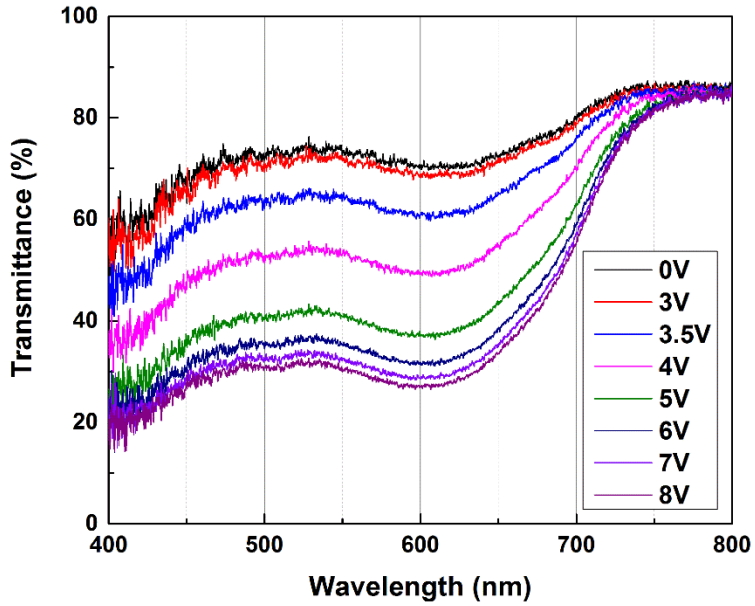

Figure 9: Voltage dependent transmittance of the LC film

The response time τ of the display can be estimated by

$$\tau \sim \frac{\gamma_1 d^2}{K\pi^2}. \tag{7}$$

Here γ_1 is the rotational viscosity, K is the effective elastic constant and d is the cell gap. To further reduce the response time of the LC film, we can use a lower viscosity LC or optimize the cell gap.

The ultimate goal of a see-through AR system is to connect the virtual world and the real world. This means the "dark" state of the LC cell cannot be completely black, and our LC film can successfully achieve this purpose, as demonstrated in Figure 10 (a) and (b). The photos were taken under normal indoor lighting. From Figure 10, we can tell that the LC cell is quite clear at the bright state (V=0). At the darkest state (8 V_{rms}), although the transmittance drops we can still distinguish the RGB colors clearly.

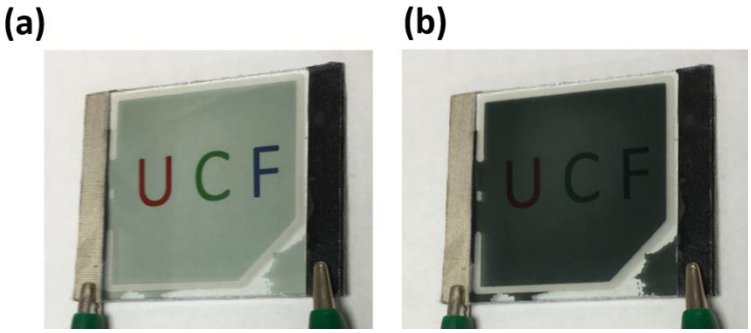

Figure 10: The performance of the LC cell at (a) bright state and (b) dark state.

Another advantage of our smart dimmer is that this film is fail-safe: when no voltage is applied, the device is in bright state, which ensures high visibility of the ambient environment even when the electronics go wrong. This ensures the users' safety.

2.3 Design Principle of the functional reflective polarizer

The Reflective polarizer, which can be mass-produced by polymer coextrusion [41], has been widely used in LCD backlight for polarization manipulation and recycling. It consists of hundreds of stacked isotropic and uniaxial layers, as shown in Figure 11 (a). The refractive index of the isotropic material is n_1, as for the uniaxial material the ordinary refractive index is n_1 and the extraordinary refractive index is n_2. The uniaxial material is aligned along the x-axis. For the light polarized along the x-axis, it sees alternating refractive index and the stack works as a highly reflective film. While for the light polarized along the y-axis, it sees only n_1 so that the structure works as a high transmittance film. In this way, the reflective polarizer would reflect the x-polarized light while transmitting y-polarized light. The reflective polarizer can be designed by the 4×4 method [42, 43] developed for analyzing uniaxial liquid crystals. However, as there is no refractive index change along the y direction, it is not possible to control the transmittance/reflectance of the y-polarized light. The most straightforward way to control the transmittance/reflectance of the y-polarized light is to introduce refractive index variation in the y

direction. However, designing such a functional reflective polarizer that controls the x-polarized light and y-polarized light simultaneously is quite challenging by the 4×4 method. To help design the functional reflective polarizer, we need to take a look at the 4×4 method, which is used for analyzing liquid crystal display, and the transfer matrix approach [44], which is used in general for thin film coating design. We can tell that the main difference between the transfer matrix approach and the 4×4 method is that in the latter we introduce polar and azimuthal angles to describe the tilt and twist deformations of the LC directors. The incurred LC reorientation will introduce polarization rotation effect into the system. However, in the case of functional reflective polarizer, the problem can be greatly simplified if we assume that the uniaxial material is oriented along x-axis or y-axis. Then the polarization rotation effect would be negligible and the design process of the functional reflective polarizer can be simplified as outlined in the following:

1. Designing two thin film coatings with different transmittance/reflectance properties using isotropic materials m_1 and m_2 with refractive index n_1 and n_2, respectively. If we name the two coatings Stack 1 and Stack 2, it is required that the two thin film coatings having the same thickness.
2. Convert the two thin film coatings to functional reflective polarizer. Compare the two stacks: at the same thickness, if both stacks have the refractive index of n_1, then for the functional reflective polarizer, at this thickness we should use material m_1. Similarly, if both stacks have the refractive indices of n_2, we should use isotropic material m_2. In addition, if for Stack 1 the refractive index is n_1 and for Stack 2 the refractive index is n_2, then we should use the uniaxial material m_3 (n_e=n_2 and n_o=n_1) with the long axis aligned along the y direction. If on the contrary, the refractive index for Stack 1 is n_2

and for Stack 2 the refractive index is n_1, then the uniaxial material should be aligned along the x direction. This conversion procedure is illustrated in Figure 11 (b).

3. Recalculate the transmittance and reflectivity of the functional reflective polarizer with the 4×4 method.
4. Fine-tune the stack design of the functional reflective polarizer.

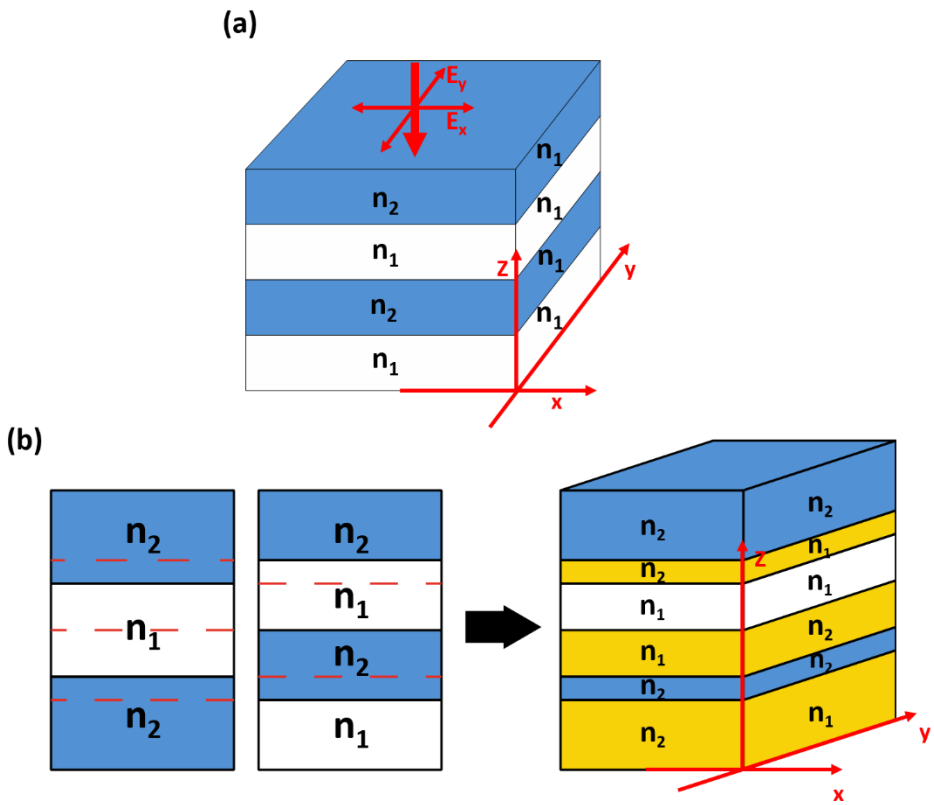

Figure 11: (a) Structure of the regular reflective polarizer and (b) the principle of converting two thin film coatings to a single functional reflective polarizer: materials m_1, m_2 and m_3 are drawn in white, blue and yellow, respectively.

With the abovementioned approach, it is possible to design the functional reflective polarizer with three materials: a uniaxial material with n_e=n_2 and n_o=n_1 and two isotropic materials with matched refractive indices of n_1 and n_2, respectively. The isotropic materials we used in our

design simulation are NOA81 (n=1.57) [45] and polyferrocenes (n=1.82) [46], and the uniaxial material is liquid crystal polymeric film (BL038, ne=1.82, no=1.57) [45]. In real fabrication, we can also select other materials as long as the refractive index matching condition is satisfied and the birefringence of the uniaxial material is large enough. The most important advantage of our approach is that there are quite a few optimization approaches for fast thin film coating designs.

2.4 Functional reflective polarizer embedded AR system for color vision deficiency

With the abovementioned approach, we designed an AR system with functional reflective polarizer for helping people with color vision deficiency (CVD). For this kind of application, the design process is mentioned in the previous section. Before we dig into the design principle, we will first give a brief introduction of color vision deficiency.

2.4.1. Origin of color vision deficiency

In the retina of the human eye, there are three types of cone cells that contribute to color vision: the L, M and S cone cells. Here L, M and S stands for long-wave, medium wave and short wave, respectively. For people with normal vision, the spectra sensitivity of their cones cells are shown in Figure 12. There are three types of CVD: 1) anomalous trichromacy where one of the pigments have shifted or altered spectra sensitivity; 2) dichromacy where one of the cone cells are not present or not working and 3) monochromacy where the viewer cannot distinguish colors [11, 14, 15]. In our thesis, we will only talk about anomalous trichromacy. A simple explanation for anomalous trichromacy is that one type of the cone cells are partially contaminated by another type, thus resulting in a spectra shift in the sensitivity curve. Depending on which kind is contaminated, there are three types of anomalous trichromacy: protanomaly, deuteranomaly, and tritanomaly. For example, in Figure 12, the red dashed lines represent a case of protanomaly where

the spectral sensitivity of the L cone cells shifts by 10nm. The larger overlap between the spectra sensitivity functions of the L and M cone cells results in inaccurate color perception.

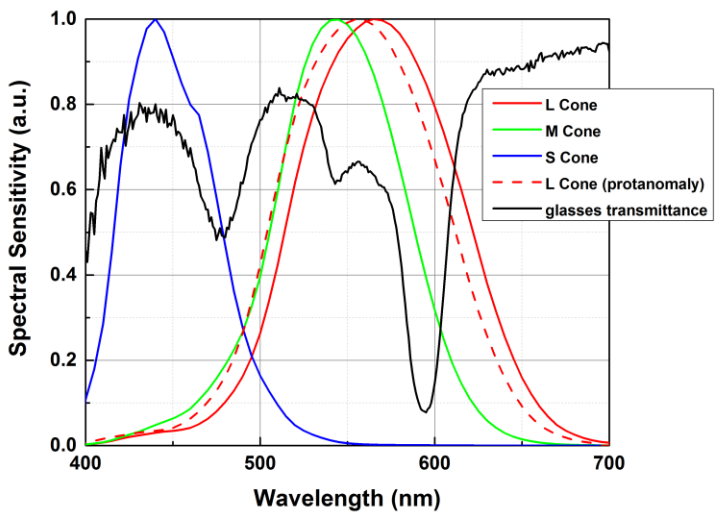

Figure 12: Spectra sensitivity functions of the L, M and S cone cells and the transmittance of the commercial EnChroma glasses for people with CVD.

The severity of anomalous trichromacy can be described by [36]:

$$S = \frac{\Delta\lambda}{20}. \tag{8}$$

Here $\Delta\lambda$ is the spectral shift in nm. From Equation (8), when S=1, i.e. $\Delta\lambda$=20nm, which implies that two of the spectra sensitivity functions completely overlap. It means the patient is with dichromacy and can only perceive two primary colors.

To help people with CVD, both computer vision based approach [36] and optics based approach have been proposed. For the latter, the basic principle is to use notched filters to reduce the overlap between the spectra sensitivity functions of the L, M and S cone cells. Also included in Figure 12, the black line is the measured transmittance data of a commercial EnChroma glass designed for people with CVD. It is obvious that there are three transmittance dips along the black

curve, and these transmittance dips help to reduce the overlap between adjacent spectra sensitivity functions.

2.4.2. Performance of our functional reflective polarizer

In our functional reflective polarizer-embedded AR system, both computer algorithm and optical approaches can be applied to help people with CVD. For the x-polarized display light, the display can be tailored based on computer algorithms to adapt to the viewer. The reflectance of the functional reflective polarizer in the x direction should be as high as possible, thus it will not temper the output display spectra and cause color inaccuracy of the displayed images. For the incident ambient light, the x-polarized part will be reflected back and cannot be perceived by the viewer. While for the y-polarization, the functional reflective polarizer functions as a notched filter to reduce the overlap between adjacent spectra sensitivity functions. Thus, the functional reflective polarizer can optically adapt the environment light for people with CVD. Based on the approach shown in Figure 11 (b), we have designed the functional reflective polarizer with its transmittance shown in Figure 13. Here we use all three materials listed in previous section. The reflective polarizer consists of 793 layers with a total thickness of 30.03 μm. Again, the thickness and alignment of each specific layer are not shown here. From Figure 13 it is obvious that our functional reflective polarizer has low transmittance (high reflectivity) for the x polarization across the visible range and it works as a notched filter simultaneously in the y direction. The overall reflectivity R_D of the x-polarized display light can be defined as:

$$R_D = 1 - T_D = 1 - \int t_x(\lambda) I_D(\lambda) d\lambda / \int I_D(\lambda) d\lambda. \tag{7}$$

In Equation (7), T_D is the overall transmittance of the display light and $I_D(\lambda)$ is the spectra of the display light. The overall reflectivity RD of the x-polarized display light calculated from Equation

(7) is ~99.0%. This indicates that with our functional reflective polarizer, both the display light and ambient light can be tailored to help those people with CVD.

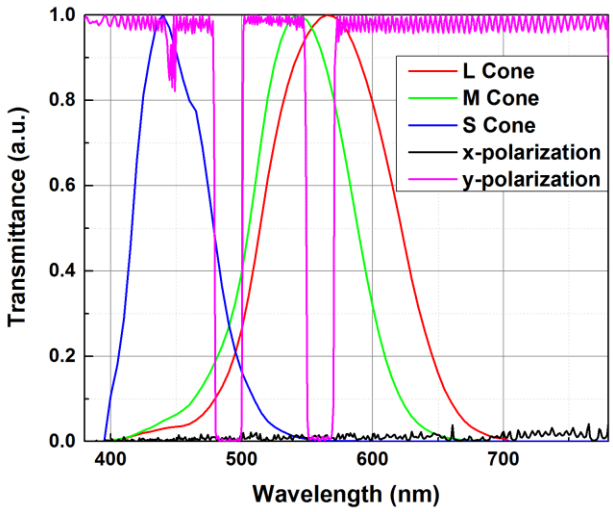

Figure 13: Spectra sensitivity function of the L, M and S cone cells and the transmittance of our functional reflective polarizer in the x and y polarization.

To evaluate the performance of our functional reflective polarizer, we simulate the images perceived by people with anomalous trichromacy with and without the functional reflective polarizer. The simulation is powered by the open source isetbio Toolbox [47] and the simulation approach is well documented in [36]. Here we summarize it as follows: 1) we obtain the RGB values of each image pixel. By specifying the light source, we can further get the spectra of each image pixel through the isetbio Toolbox. 2) We can simulate the perceived spectra of each pixel after the functional reflective polarizer. Then an image perceived by people with normal vision can be reconstructed based on the spectra. For people with anomalous trichromacy, the perceived image can be deduced from the image perceived by people with normal vision based on matrix manipulation described in [36]. Here we assume the ambient environment is a close-up view of a

ladybeetle. The simulation image is taken from Wikimedia Commons and here we assume the image is displayed by the OLED panel specified as "OLED-Samsung.mat" in the isetbio Toolbox. In our simulation, we consider two cases: (1) the severity of anomalous trichromacy is 0.4 (8nm spectral shift), which means the anomalous trichromacy is not very severe and (2) the severity of anomalous trichromacy is 0.8 (16nm spectral shift) where the CVD is quite severe. For the first case, the simulation results without and with the functional reflective polarizer are illustrated in Figure 14 (a) and (b), respectively. Our functional reflective polarizer helps people with anomalous trichromacy to see more saturated colors when the anomalous trichromacy is not severe. For the second case, the perceived images without and with functional reflective polarizer are demonstrated in Figure 14 (c) and (d), respectively. By comparing these two figures, we find that even when the anomalous trichromacy is severe our functional reflective polarizer is still helpful to enhance the image contrast.

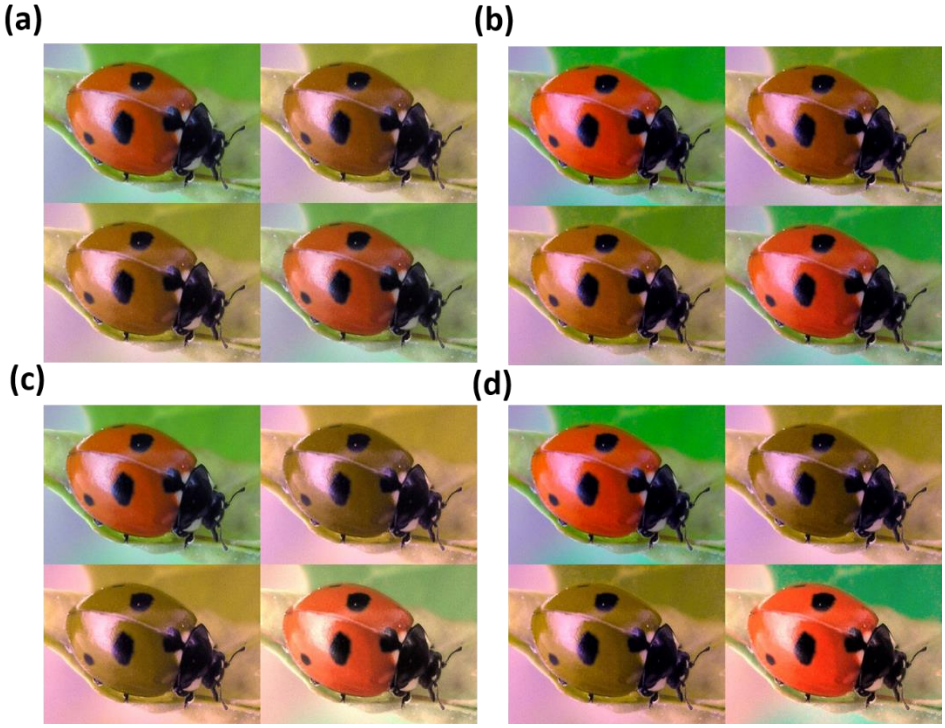

Figure 14: (a) The perceived image without functional reflective polarizer. From upper left to bottom right, the images correspond to people with normal vision (upper left), protanomaly (upper right), deuteranomaly (bottom left) and tritanomaly (bottom right); (b) the perceived image with functional reflective polarizer. For (a)-(b), the spectral shift is 8nm. (c) The perceived image without functional reflective polarizer when the spectral shift is 16nm and (d) the perceived image with functional reflective polarizer when the spectral shift is 16nm.

2.5 Summary

In summary, we have developed a high ACR AR system for people with CVD by combining a smart dimmer with a functional reflective polarizer. The smart dimmer is based on the guest-host LC approach and has three advantages: 1) fast response time, 2) high ambient contrast and 3) fail-safe. The design principle of the functional reflective polarizer is well

explained. The functional reflective polarizer demonstrates high reflectivity in one polarization and works as a notched filter in the other polarization.

CHAPTER THREE: DUAL PANEL FOR HIGH DYNAMIC RANGE DISPLAYS

As mentioned in Chapter One, to achieve high dynamic range we should improve the dark state and peak brightness of the display simultaneously. For example, the luminance of bright state should be > 1000 nits, while dark state should be < 0.01 nits. In other words, the effective CR is over 100,000:1. For an organic light-emitting diode (OLED) display, it is fairly easy to get true black state, but to obtain a brightness over 1000 nits would lead to compromised lifetime [48]. On the other hand, with the help of high power LEDs, it is relatively easy to boost an LCD's peak brightness to 1000 nits, but to lower the dark state to < 0.01 nits is challenging. A typical CR of a multi-domain vertical alignment (MVA) LCD is ~5000:1, which is about 20x lower than what HDR demands. To improve dark state, local dimming technique has been commonly used [49, 50].

A key challenge with the present local dimming approach is that it cannot be pixelated, thus requires complex algorithms [51] to mitigate the image artifacts, such as halo and clipping. To avoid the computational complexity, a pixel-by-pixel local dimming approach is preferred.

In this chapter, we demonstrate a HDR LCD with two cascaded panels. In fact, dual-layer or even multi-layer LCD has already been widely used in 3D display, volumetric display and light field display [52-54], but few reports are focused on their electro-optical properties. Here, we perform systematic investigations on the dual-panel HDR LCD system, with special emphases on contrast ratio, operation voltage, response time, viewing angle, and Moiré effect. Our analysis and test cell experimental results indicate that we are able to achieve CR >1,000,000:1 (limited by the noise of our photodiode detector), low operation voltage (~5V), and pixel-level local dimming. To eliminate the Moiré patterns induced by the cascaded TFT backplanes, we introduced a

polarization dependent scattering film (PDSF). Potential concerns for the dual-layer system are discussed, such as increased panel thickness, weight, cost, misalignment effect, and reduced optical efficiency. We believe such a HDR LCD would find widespread applications for medical imaging, art designing, movies, and vehicular displays.

3.1 Device configuration and working principles

The device configuration of the dual panel system is shown in Figure 15. The system consists of a master display panel (LCD #2) and a pixelated dimming panel (LCD #1). In principle, any two LC modes can be paired up to construct the display [55-57], for example, VA and 90° TN (twisted nematic), VA and FFS (fringe-field switching), FFS and TN, two TNs, or two FFSs, just to name a few. However, considering the viewing angle, color shift, and cost, we choose FFS as master display and black-and-white TN (the same dimension but without color filters) as local dimmer. TN is a normally-white broadband half-wave plate [56], that means, at $V = 0$ the incident white light passes through the TN panel and reaches the master display with high efficiency. If the local dimming is on demand, we can apply different voltages (through TFTs) to those chosen pixels to control their transmittance. While for the FFS panel, it shows excellent image quality, including wide viewing angle, small color shift, weak gamma shift, and pressure resistance for touch panels. Therefore, we put it in the viewer side. Later, we will use the FFS/TN test cell results to illustrate the operation principles. Let us assume the contrast ratio of the two LCD panels is CR_1 and CR_2, respectively. Then for the cascaded display system, the effective contrast ratio should be CR_1*CR_2 [1]. A typical CR for FFS LCD is ~2000:1 and TN is ~800:1, thus ideally the intrinsic CR of dual panels should be 1,600,000:1. Another advantage of this design is pixel-level local dimming, similar to OLED, if two panels are aligned well. Of course, there are some drawbacks,

like decreased efficiency, increased cost, and misalignment issue. We will discuss these factors in detail later.

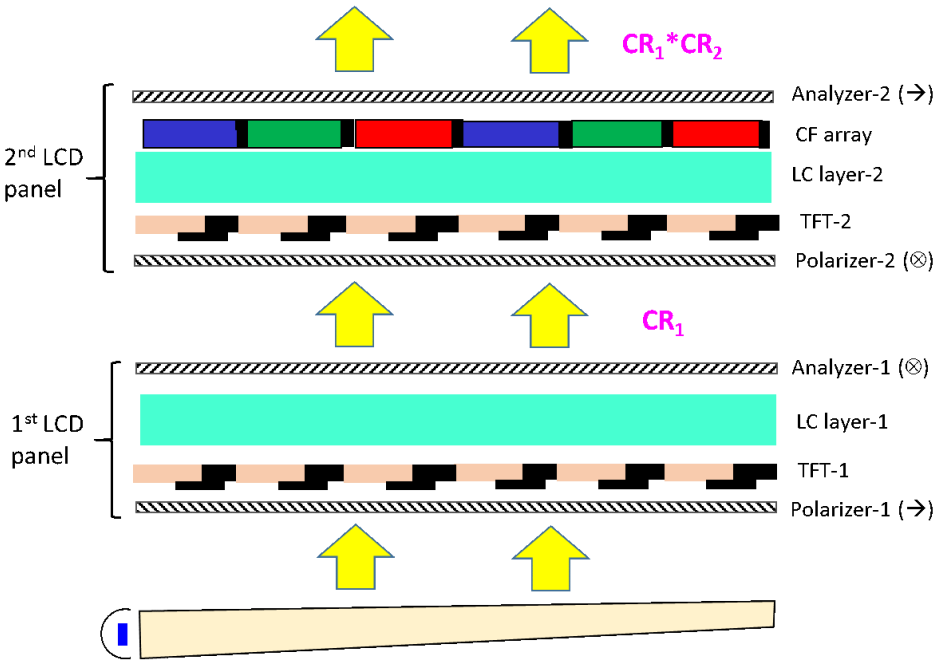

Figure 15: Device setup of the dual panel display system.

3.2 simulation and experimental results

Based on the dual panel concept, we conducted simulation and experimental analysis. Below are the results:

3.2.1 VT Curve

In experiment, we prepared one TN test cell with cell gap d = 5 μm and one FFS test cell with cell gap d = 3.5 μm. The employed LC (MLC-6686, Merck) material parameters are: birefringence Δn = 0.0983 @ λ = 550 nm and dielectric anisotropy $\Delta\varepsilon$ = 10.0 [58] A He-Ne laser with λ = 633 nm was used as probe beam. During measurement, the LC cell was driven by a square-wave voltage at 1 kHz frequency. The applied voltage was controlled by a LabVIEW (National

Instruments) system. The measured voltage-dependent transmittance (VT) curves for both cells are plotted in Figure 16. As expected, the TN test cell shows ~100% transmittance (normalized to two parallel polarizers) and the dark state occurs at V = 3 V_{rms}. It is a perfect candidate for backlight local dimming. While for the FFS test cell (electrode width = 4 µm, and electrode gap = 3 µm), its peak transmittance at λ = 633 nm is 73.6% and V_{on} = 4.2 V. If a low $\Delta\varepsilon$ LC mixture is employed, higher transmittance can be obtained, but at a slightly higher voltage [58].

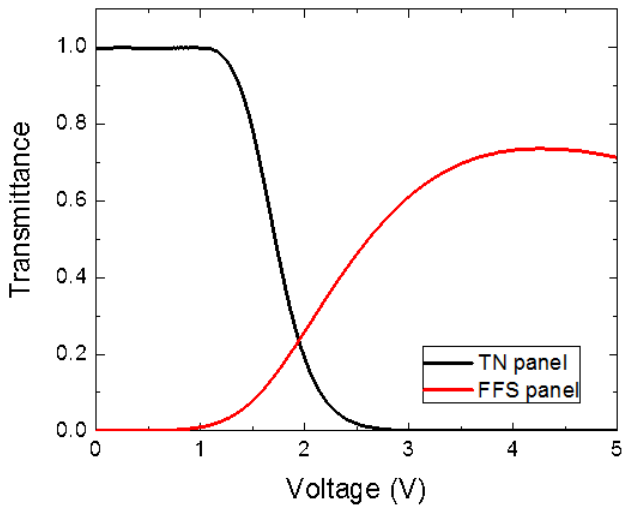

Figure 16: Voltage-transmittance curve measurement of the TN and FFS cell.

3.2.2 Contrast ratio

Next, we measured the contrast ratio of these two test cells. Results are CR_{FFS} = 4625:1 and CR_{TN} = 2172:1. When we placed these two cells in sequence (TN is closer to the light source), in principle the CR should reach 9,263,580:1 (CR_{FFS}*CR_{TN}), but in experiment we only obtained CR = 1,102,564:1 when the TN cell was driven at 3 V_{rms}. This result is 8.4x smaller than the theoretical value, but still much higher than the required 100,000:1 requirement for HDR displays. The reduced CR could be limited by the sensitivity of the photodiode detector we employed. Please

note that, here, high extinction ratio (~ 18,000:1) polarizers were adopted, and the measurement was performed using He-Ne laser (λ = 633 nm). As a result, the obtained CR would be higher than the traditional value using white backlight.

3.2.3 Response time

The measured response time of the FFS and TN cell is shown in Figure 17 (a) and (b), respectively. Due to the small twist elastic constant [59], FFS cell exhibits relatively slower response time (rise time: 24.5 ms, decay time: 21.6 ms); while for TN cell, the measured response time is fairly fast (decay time: 4.4 ms, rise time: 9.7 ms). Then we combine FFS and TN cell together, and investigate the response time of dual-panel system. Results are plotted in Figure 17 (c), where rise time is 19.0 ms, and decay time is 6.4 ms. Interestingly, both rise and decay time are improved as compared to single FFS cell, especially for decay time (21.6 ms vs. 6.4 ms). It means TN panel helps to accelerate the total transition process efficiently. If we use a thinner cell gap with higher Δn yet low viscosity LC, faster response time (< 2 ms) can be realized [60-62]. In this way, the motion picture response time of the display would be comparable to that of an OLED, leading to much suppressed image blurs. [63, 64].

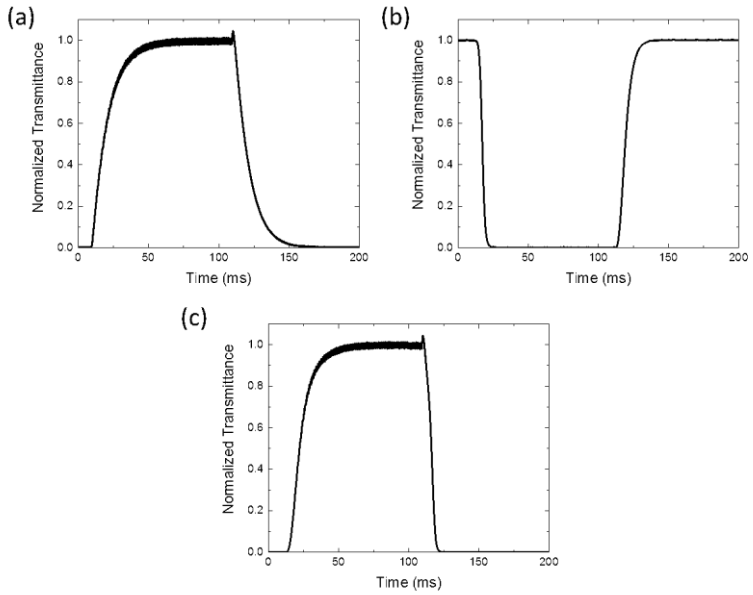

Figure 17: Measured response time for (a) single FFS cell, (b) single TN cell, and (c) combined FFS + TN cell.

3.2.4 Viewing angle

Figure 18 (a) shows the simulated isocontrast contours for a conventional TN LCD. The highest CR is about 1200:1, and it drops gradually as the viewing cone increases. For some azimuthal angle, say 230°, it is less than 10:1, which means the image quality is degraded greatly. For FFS LCD [Figure 18 (b)], its CR could reach ~2500:1, but still drop to 100:1 at large viewing angles.

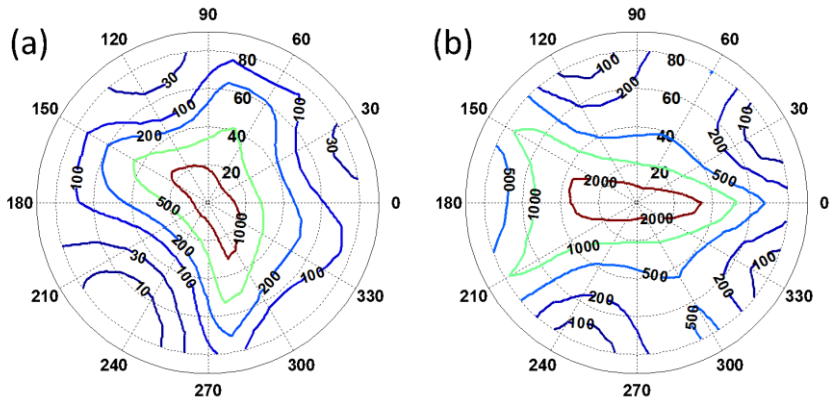

Figure 18: Calculated isocontrast contour for (a) single TN panel and (b) single FFS panel.

When we cascade them together, the CR exceeds 1,000,000:1 within the ~20° viewing cone, as shown in Figure 19. Even for the entire viewing zone, CR still keeps over 1000:1. If we define the HDR requirement as 100,000:1, then the viewing angle in the horizontal direction is extended to about 60°. Meanwhile, since we use FFS as master display panel, its color shift and gamma shift are very weak.

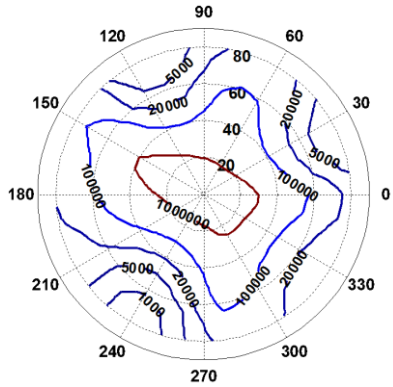

Figure 19: Simulated isocontrast contour for the cascaded FFS and TN panels.

3.3 Potential problems of the dual panel approach

As above mentioned, dual LCD panels show great advantages in contrast ratio and viewing angle. However, some challenges remain to be solved. The first one is increased cost, because two panels are used. Fortunately, the portion of panel cost in total price is not high. For example, in a

5’’ FHD smartphone, the LCD panel is only $25 or lower. Compared to the total price $500 of a smartphone, the display part only occupies ~5%. For large size TVs, this portion is higher, but still acceptable. On the other hand, cost is not a big issue for some high-end devices, like medical diagnosis, movie directing, photographers, universe detecting, art designers, etc.

Increased thickness is another concern for dual LCD panels. For a conventional edge-lit LCD panel, the thickness is about 1.6 mm. And for direct-lit technology with local dimming, thickness is ~5 mm. As shown in Figure 15, in our design, one more LC panel is added, consisting of two polarizers (130 µm × 2), two substrates (200 µm × 2), LC layer (4 µm), and compensation films (150 µm). The total thickness is about 0.9 mm. Therefore, for the whole device it is 2.5-mm thick, which is still ~2x thinner than the direct-lit display.

The other issue for dual LCD panels is decreased efficiency, which mainly results from the additional polarizers. Because of the absorption of polarizer, about 25% optical efficiency is sacrificed. At the same time, the electrical power consumption would increase or even doubled as compared to a single panel.

Next issue is misalignment. If two LC panels do not align precisely, then the image would be distorted. Fortunately, this issue could be mitigated from image processing part. Guarnieri et al. developed a novel splitting algorithm to minimize the errors caused by misalignment [65, 66]. Based on their analysis, the images could still remain good quality even though there is 3-pixel spatial shift between two LCD panels.

3.4 Reducing the Moiré effect with polarization dependent scattering film

When two LCD panels are placed in sequence, Moiré effect appears because of the patterned TFT backplanes. To reduce this effect, a strong diffuser is often needed. In this case, the

output light from the first panel will be depolarized, degrading the whole performance. To solve this issue, we proposed a new structure design using a polarization dependent scattering film (PDSF), as depicted in Figure 20. The only difference is that a PDSF is added between two LCD panels, to replace the conventional strong diffuser. This PDSF exhibits a unique property: polarization dependent scattering [67, 68]. For example, PDSF would scatter the s-wave strongly, whereas transmitting the p-wave. With this unique scattering property of PDSF film, Moiré effect would be mitigated while keeping high CR for dual LCD panels.

The working mechanism could be briefly described as follows. For bright state, there is strong s-polarized light from the first LCD panel. As described above, it would be scattered by the PDSF, then entering the second LCD panel. As a result, Moiré effect is mitigated. While for dark state, quite weak p-polarized light traverses through the first TN panel, and enters PDSF. In this case, it could go through without scattering; its polarization state is conserved. Namely, no depolarization effect occurs. Thus, high CR is realized. Clearly, in real applications, the transmittance and scattering properties of PSDF need to be optimized in order to balance the Moiré effect reduction and high contrast ratio.

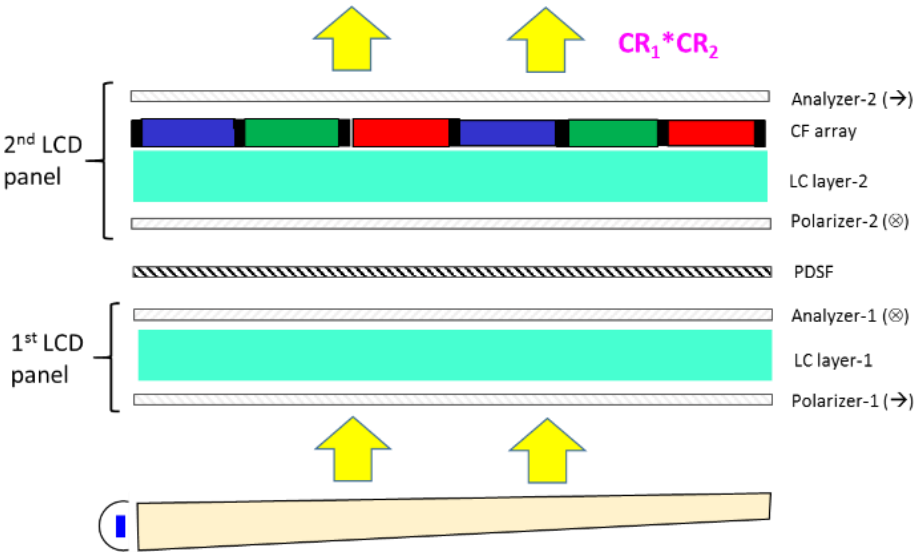

Figure 20: Schematic diagram for the proposed structure using polarization dependent scattering film (PDSF).

Experimentally, we prepared a mixture consisting of BL038 (95.6 wt%), RM257 (4.2 wt%) and Irg651 (0.2 wt%). Homogeneous cell with cell gap d = 12 μm was employed. Then LC test cell was first cured using 365 nm UV lamp for 30 sec with 5 mW/cm^2. After that, we applied 20 V to the cell, and cured again for 1 hour with the same UV intensity. The detailed fabrication process and physical mechanism of PDSF could be found in [22]. The measurement setup is depicted in Figure 21. A He-Ne laser with λ = 633 nm was used as probing beam and the acceptance angle of detector was 4.5°.

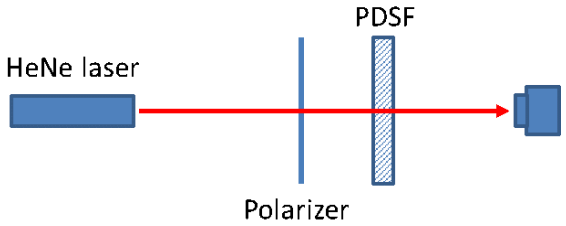

Figure 21: Experimental setup for PDSF measurement.

When we rotate the PDSF, the light intensity after PDSF is changed because the scattered or transmitted light is tuned. The measured result is plotted in Figure 22. The peak transmittance is 75%, while in the scattering state the transmittance drops to 2.6%. The CR is about 28.6:1. Also, we compared their spectrum at two states, as shown in Figure 23. As the wavelength decreases, the scattering gets stronger, leading to decreased transmittance. For practical applications, the recipe of PDSF and its curing conditions have to be optimized based on different requirements.

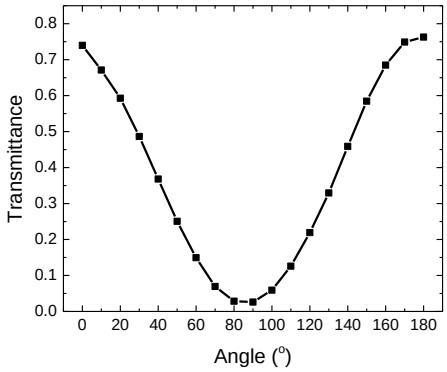

Figure 22: Transmittance as a function of polarization angle.

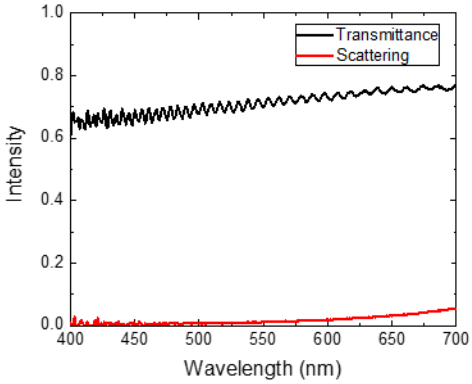

Figure 23: Measured transmission and scattering spectra of the PDSF.

3.5 Summary

In summary, to solve the contrast ratio challenge of HDR display. We have proposed a dual panel approach. Besides high contrast, the system has the advantage of pixel level local

dimming. The challenges of this approach, such as the misalignment issue and system compactness are also discussed. At the same time, the PDSF approach has been investigated and analyzed to suppress the Moiré effect.

CHAPTER FOUR: QUANTUM DOTS FOR WIDE COLOR GAMUT HIGH DYNAMIC RANGE DISPLAYS

As mentioned in Chapter One, HDR displays also come with more saturated colors. The color a display can present is described by the color gamut. The color gamut is described as the triangle confined by the color primaries in the CIE1931 color diagram. A larger color triangle indicates the display can produce more saturated colors. Among these color gamuts, some of the most widely used color gamuts are: sRGB, which is the de-facto standard for online images; Rec. 709, which is a variety of sRGB standardized for high definition TV (HDTV) [69]; DCI-P3, which has been used by the entertainment industry and is gaining momentum in consumer electronics [70]; Adobe RGB, which is quite popular among professional photographers because of its deep and saturated green colors [71]; and the latest Rec. 2020 color gamut [23]. The Rec. 2020 color gamut became the standard for ultra-high definition (UHD) and HDR displays for three reasons: 1. The Rec. 2020 color gamut can enclose the color primaries of all the other four standards [72]; 2. The color triangle of Rec. 2020 cover up to 99.9% of the Pointer's gamut [73], which indicates displays capable of handling Rec. 2020 can faithfully reproduce the natural object colors. Finally yet importantly, the Rec. 2020 standard can be physically realized through RGB laser sources [72, 74]. These color gamuts are plotted in Figure 24.

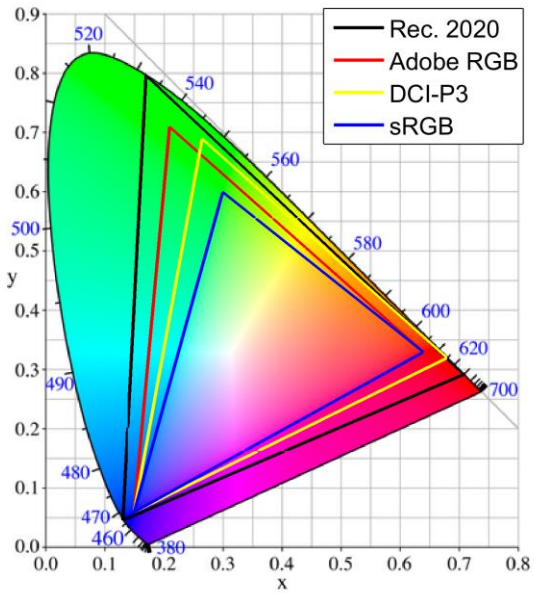

Figure 24: Typical color gamuts used in display industry.

Although the Rec. 2020 standard can be realized with monochromatic laser sources, for a real display, laser sources are expensive and the speckle problem [75] has not yet been fully solved. In this sense, it is preferred to find non-monochromatic light sources to realize the Rec. 2020 standard. Among these candidates, quantum dots (QDs) have attracted much attention because of their narrow and tunable emission spectra [76].

There are two approaches to use QDs for displays: photoluminescence (PL) quantum dots for liquid crystal display (LCD) backlight [25, 77, 78] and electroluminescence (EL) quantum-dot light emitting diodes (QLEDs) [31, 79-82]. In this thesis, we will discuss how to realize the Rec. 2020 standard with both approaches, and the tradeoff between color gamut and optical efficiency.

4.1 Display system evaluation

Before we dive into performance evaluation of different displays, we should first establish the evaluation metrics. The first and most important evaluation metric is color gamut, which is determined by the maximum colors a display can reproduce based on Rec. 2020. While the system colorimetry of Rec. 2020 [23] shown in Table 1 is quite straightforward, the definition of color gamut is sometimes confusing and misleading. The most accurate way is to calculate the color volume in a three-dimensional (3D) color space or color appearance model, such as the CIELAB or CIECAM02. However, the gamut calculation in 3D color space is both complex and unintuitive and no one actually do this in the display industry. Instead, the gamut calculation is based on two-dimensional (2D) color diagrams. Some manufactures define the area ratio as the color gamut, which compares the RGB triangular area of a display with the triangular area of the Rec. 2020 standard, namely:

$$Color\ Gamut\ Area = \frac{A_{display}}{A_{standard}}. \tag{8}$$

Whereas others define the coverage ratio as the color gamut, which can be expressed as:

$$Color\ Gamut\ Area = \frac{A_{display} \cap A_{standard}}{A_{standard}}. \tag{9}$$

What makes the situation even more confusing is that CIE 1931 and CIE 1976 are used simultaneously when calculating the color gamut, although these two color spaces are quite different. As pointed out in [24] the coverage ratios in CIE 1931 and CIE 1976 are rather inconsistent, and the coverage ratio calculated with CIE 1931 is more consistent to the Rec. 2020 volume coverage ratio in color appearance model CIELAB, CIELUV and CIECAM02. In this

sense, we will use the coverage ratio in CIE 1931 as the metric, while including the coverage ratio in CIE 1976 as a reference. We will discuss more about the color space selection later in this chapter.

Table 1: System colorimetry of Rec. 2020 standards

	Chromaticity coordinates (CIE 1931)	x	y	Corresponding wavelength (nm)
Primary colors and Reference white	Red Primary	0.708	0.292	630
	Green Primary	0.170	0.797	532
	Blue Primary	0.131	0.046	467
	Reference White (D65)	0.313	0.329	/

The other metric should describe how efficient the display system is. Here we emphasize on optical efficiency because realizing a wide color gamut is mainly to optimize the output spectra power density (SPD). The SPD directly determines the luminous efficacy of radiation (*LER*) of the system [77]:

$$LER = \frac{K_m \int S_{out}(\lambda) V(\lambda) d\lambda}{\int S_{out}(\lambda) d\lambda}. \tag{10}$$

In Equation (10), $S_{out}(\lambda)$ is the SPD of the output light, $V(\lambda)$ is the standard luminosity function, and K_m=683 lm/W is the LER of the ideal monochromatic 555-nm source. As the *LER* is only determined by the light spectra, it sets the theoretical limit for the total efficiency of a display.

For a non-emissive display such as LCD, the SPD of the backlight ($S_{in}(\lambda)$) and the actual output light ($S_{out}(\lambda)$) can be modulated dramatically, depending on the transmission characteristics of the system. To quantify the transmission characteristics of the system, we introduce the transfer efficiency (*TE*) of the system as:

$$TE = \frac{\int S_{out}(\lambda)d\lambda}{\int S_{in}(\lambda)d\lambda}. \tag{11}$$

The total light efficiency (*TLE*) of the system is:

$$TLE = LER \bullet TE = \frac{K_m \int S_{out}(\lambda)V(\lambda)d\lambda}{\int S_{in}(\lambda)d\lambda}. \tag{12}$$

For our analysis below, the main evaluation metrics are color gamut and *LER*. While evaluating a non-emissive display, we will also discuss its *TLE*.

The evaluation process can be outlined as follows: assuming a display with RGB primary colors, the SPD of each primary color can be written as $S_{out,i}(\lambda)$ ($i=r,g,b$), and the total output light spectra reaching the system white point is:

$$\begin{aligned} &S_{out}(\lambda) = RS_{out,r}(\lambda) + GS_{out,g}(\lambda) + BS_{out,b}(\lambda). \\ &R + G + B = 1 \end{aligned} \tag{13}$$

In Equation (13), R, G and B represent the weighting ratio of the corresponding color; they are so determined that the white point of the display is D65.

There are quite a few models [83] to simulate the emitting spectra of the QDs, for both EL and PL QDs, a good enough model is the Gaussian model, namely the normalized SPD can be well fit by a Gaussian function:

$$S_i(\lambda, \lambda_0, \Delta\lambda) = e^{-4ln2\frac{(\lambda-\lambda_0)^2}{\Delta\lambda^2}}. \tag{14}$$

Here *i* stands for R, G and B, respectively, λ_0 is the central wavelength, and $\Delta\lambda$ is the linewidth of the emission spectra (full width half maximum).

With Equations (9)-(14), we can calculate the color gamut and *LER* of the display, and for a non-emissive display, we can also calculate the *TLE* of the system. We can then optimize the color gamut by varying the QD's central wavelength λ_0 and linewidth $\Delta\lambda$. Several approaches have been developed to optimize the color gamut of a display; the most convenient one is the multi-objective optimization that combines both *LER* (*TLE*) and color gamut. The detailed approach have been described in [77, 84], and the results will be discussed later.

As an example, we calculate the *LER* of an ideal laser display with three monochromatic light sources, which covers 100% color gamut of Rec. 2020. The resultant R, G and B are 39.7%, 30.8% and 29.5%, respectively, and *LER* is 273.9 lm/W. This LER serves as benchmark for our comparison.

4.2 Wide color gamut QD-enhanced LCD

Recently, QD-enhanced LCDs are emerging. Contemporary QD-LCDs use either on-edge approach [85] where the quantum dot is placed on the edge of the light guide plate or film approach [86] where the quantum dots are embedded in an optical film on top of the light guide plate. For these two approaches, they both use a blue LED to pump the red and green quantum dots. The generated light is modulated by the LC layer (sandwiched between crossed polarizers), and passes through the color filters (CFs). Besides the spectra of the backlight, the color of the display can be affected by the transmittance of the color filters and the wavelength dispersion of the LC material and polarizers. However, in comparison with color filters, the dispersion of the LC material and polarizers has negligible effect on the color performance [87] This is because for different LC modes, although the overall transmittance slightly depends on the wavelength, the shape of these transmission curves remain quite similar [25]. If we consider the transmittance of the RGB color

filters and the LC, we can say that the color filters play the major role in terms of reshaping the output light spectra. The LC materials we use here are the same as [77].

Next, we examine how to achieve wide color gamut with two commercial color filters: CF1 is commonly used for TVs because of its relatively high transmittance, especially for green and blue. However, the crosstalk between different channels is larger than that of CF2, as shown in Figure 25 (a). Obviously, it will be more difficult to obtain wide color gamut with CF1. To confirm this and see how wide a color gamut we can get, we plot the Pareto front [88] of the LCD with these two CFs and for two commonly used LC modes: n-FFS for mobile displays and MVA for large-size TVs. The Pareto front determines the optimal value of a display and all the solutions will fall either on or below the Pareto Front.

Contemporary Cd-based QDs usually have a linewidth between 20-30 nm [89], and thus it is plausible to select 20nm and 30nm as the boundary conditions for linewidth. Meanwhile, for LCD applications, the blue part is achieved through blue LED and its linewidth is about 20nm. Because of this reason, the two boundary conditions for RGB QD-LCD in terms of linewidth are 1) $\Delta\lambda_r=\Delta\lambda_g=30$nm, $\Delta\lambda_b=20$nm; and 2) $\Delta\lambda_r=\Delta\lambda_g=\Delta\lambda_b=20$nm. We then vary the central wavelength λ_0 and the R, G, B ratios. All the results below are calculated in the CIE 1931 chromaticity diagram and the reference white point is always D65. Of course, we can also set the linewidth of the R, G and B colors as variables to match the Rec. 2020 color gamut, and these Pareto fronts will fall between the two boundaries. These results will be discussed later.

Figure 25 (b) depicts the simulated Pareto Front: the solid lines represent the upper-limit, i.e. the linewidth is 20nm for R, G and B colors, whereas the dashed lines represent the lower-limit boundary conditions where the linewidth is 30nm for red and green, and 20nm for blue. The red

and green lines in Figure 25 (b) represent the n-FFS mode whereas the blue and black lines represent the MVA mode. The red and blue lines use CF1 while green and black lines use CF2. From Figure 25 (b) we can deduce that 1) wider color gamut always trades off with lower *TLE*. 2) Even though the color gamut is jointly determined by the CFs, the transmittance of the LC cell, and the linewidth of the primaries, their importance is different. The CFs play the most important role while the transmittance of the LC cell is least important. In the meantime, a light source with narrower linewidth (red and green QDs and blue LED) helps widen the color gamut. 3) Comparing the red solid line with the blue solid line, the transmittance of the LC has little to do with the color gamut. However, different LC modes can dramatically affect the *TLE* of the system. For the n-FFS mode, its average *TLE* is 27.4 while for the MVA mode its average *TLE* is 18.7, which is quite close to the transmittance difference of the n-FFS and MVA modes (95% vs. 70%). 4) Comparing CF1 with CF2, displays with CF1 usually have higher *TLE*, but it is difficult to get wide color gamut. For n-FFS, the widest color gamut we can get with CF1 and CF2 are summarized in Figure 25 (c)-(d) and Table 2 (the linewidths of the three colors are all 20nm). In the meantime, we can clearly see that in comparison with CF1, CF2 sacrifices 24% *TLE* but only gain 2.7% in color gamut. This tradeoff is not worth taking. For MVA, the results are quite similar except that the *TLE* is lower. The reason that MVA has a lower *TLE* than n-FFS is due to its relatively large electrode size (for TVs), as a result, the dead zone area is larger [90], which in turn lowers the transmittance. While for n-FFS (for smart phones), its transmittance can reach 95% [57, 62, 91].

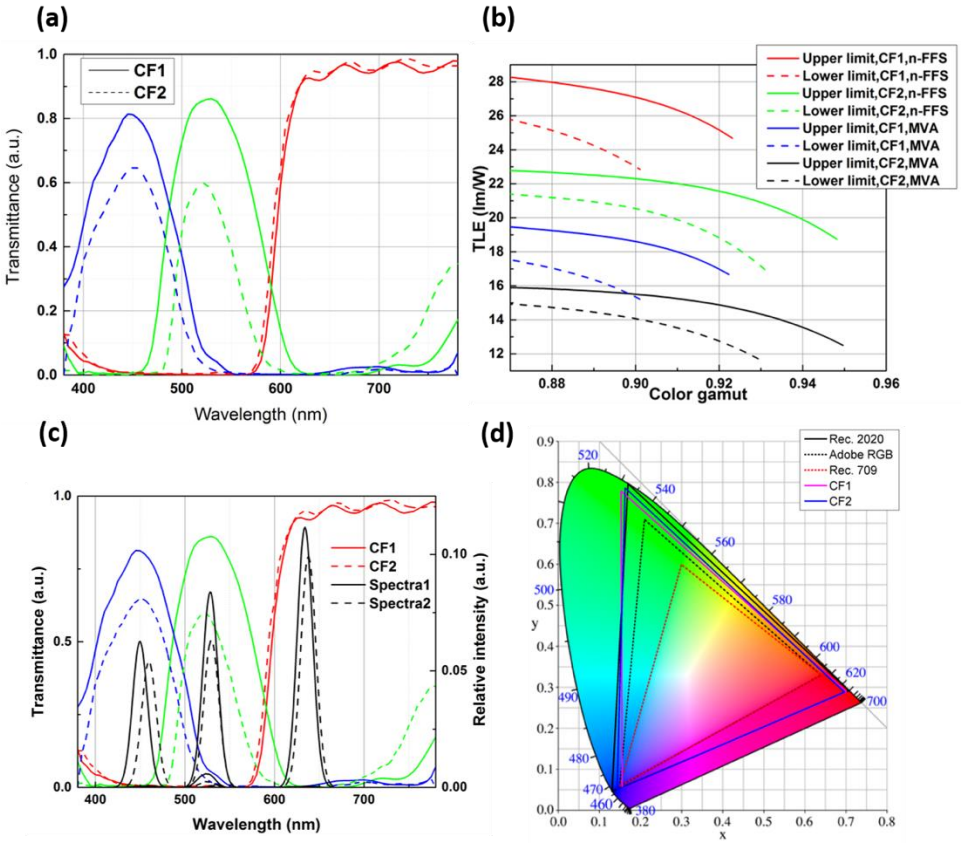

Figure 25: (a) The transmittance of two color filters; (b) the Pareto front of the QD-LCDs with different boundary condition, LC mode and color filters; (c) the transmittance and the corresponding optimized output spectra for the two color filters; and (d) the simulated color gamut for the two optimized output spectra.

From Figure 25 (c)-(d), the red primary is quite close to the Rec. 2020 standard, while the green and blue primaries still fall short, especially the green. This results from the crosstalk between green and blue color filters. There are two approaches to resolve this problem: 1) reducing the linewidth of the QD and blue LED further, and 2) redesigning the color filters.

Table 2: Optimized values of the two wide color gamut n-FFS LCDs with CF1 and CF2, respectively.

CF type	CF1	CF2
TLE (lm/W)	24.6	18.7
Color Gamut	92.3%	94.8%

In the first approach, let us make a bold assumption that the linewidth of the three primary colors can be further reduced to 10nm, which has not been achieved by commercial materials yet. Table 3 lists the simulated results. We find that even with such a narrowband light source, the color gamut improvement is insignificant because of the crosstalk between different color filters. A more promising approach is to narrow the bandwidth of color filters.

Table 3: Optimized values of two wide color gamut MVA LCDs with 10-nm-linewidth primary colors for CF1 and CF2, respectively.

CF type	CF1	CF2
TLE (lm/W)	17.6	13.3
Color Gamut	94.1%	96.0%

Several approaches have been proposed to reduce the crosstalk between different color channels [92, 93]. Figure 26 (a) shows one of the newly proposed color filters [93]: the red color filter is optimized to reduce the long transmission tail at the blue-green region. However, the crosstalk between green and blue color filters is still quite severe. Designing an even wider color gamut QD-LCD is tricky for two reasons: 1) Of course we can enlarge the color gamut by using deeper blue and red, or shifting the cutoff wavelength of the color filters, however, these do not necessarily mean large color gamut coverage as the area might overlap less with the Rec. 2020

standard. Thus predicting the color gamut is more difficult. 2) The white point has to occur at D65, which gives us less design freedom.

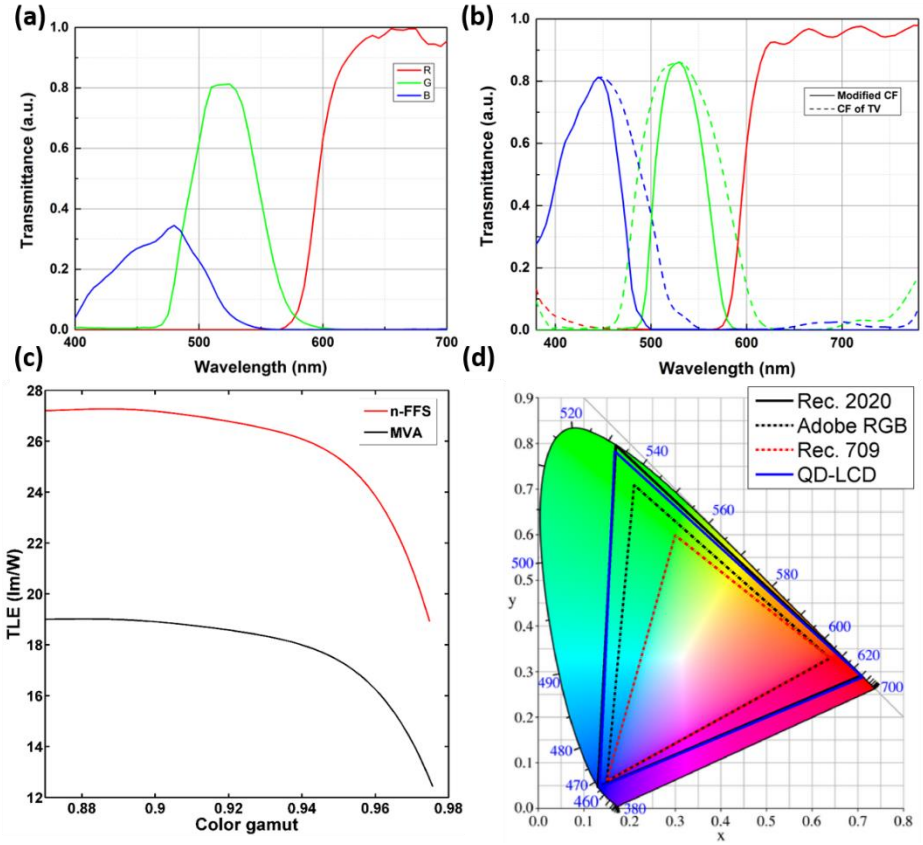

Figure 26: (a) One of the proposed CFs with wide color gamut. (b) The transmittance of our modified CFs based on the CFs for TV. (c) The Pareto front of the wide color gamut display with our modified CFs and all the linewidths of the three primaries are set at 20nm, for both MVA and n-FFS modes. (d) Simulated color triangle of the wide color gamut QD-LCD (MVA mode).

The solid lines in Figure 26 (b) are the conceptual color filters we designed. In comparison with the commonly used color filters for TVs (dashed lines), our modified color filters exhibit a wider color gamut based on following two important design features: 1) The transmittance curves are much cleaner as the “tails” in the red and blue region diminish; this is essential because these tails degrade the purity of the color primaries. 2) The transmission band of both blue and green

color filters is narrowed to minimize the overlapping between different color channels. Figure 26 (c) depicts the Pareto Front for MVA and n-FFS modes. With the proposed color filters and setting the linewidths of all three primary colors to 20nm, we can achieve ~97.6% of the Rec. 2020 color gamut in CIE 1931, or ~98.6% in CIE 1976. The TLE of MVA is ~40% lower than that of n-FFS. Such a wide color gamut display can reproduce most of the colors that Rec. 2020 demands [94]. If we inspect the color triangle in Figure 26 (d), we can determine that the color triangle overlaps well with the Rec. 2020 standard except that the green deviates slightly. Table 4 lists the optimized parameters for both MVA and n-FFS.

Table 4: System parameters of the widest color gamut we can get with the modified color filters, for both MVA and n-FFS modes.

LC mode		MVA	n-FFS
	Red	637.8	638.3
	Green	530.9	530.5
	Blue	469.1	467.6
TLE (lm/W)		12.1	18.3
Color Gamut		97.6%	97.5%

If we compare Table 2-4, we can find the tradeoff between color gamut and *TLE* is quite significant. For example, for the n-FFS mode shown in Table 2 and Table 4, when the color gamut widens from 92.3% to 97.5%, which is 5.6% increase, the *TLE* drops from 24.6 to 18.3, which is 25.6% decrease in optical efficiency. Such a sacrifice may not be worth taking because power efficiency is a critical issue for all displays. For practical applications, we need to balance color gamut with optical efficiency. We will give a more detailed discussion in a later section.

Meanwhile if we compare the optimized wavelengths in Table 4 to those listed in [95], which are optimized to cover the Pointer's Gamut, we find that these two results are quite close except for the green primaries. This similarity comes from the fact that Rec. 2020 is also designed to cover the Pointer's Gamut. As for the green primaries, they are a little bit different because of the greatly modified green color filter in our design.

4.3 Wide color gamut RGB QLED

QLED has long been considered as a potential candidate for next generation display because it offers narrow linewidth and selectable central wavelength. Moreover, the device structure is similar to that of contemporary OLED. Consequently, QLED is also suitable for flexible displays and its manufacturing is compatible to OLED. Previously, QLEDs are regarded as a future technology because of its relatively low external quantum efficiency (EQE) and relatively short lifetime. Recently, with the demonstration of high EQE and long life quantum dots, there is renewed strong interest on QLED. Figure 27 (a) shows the typical device structures of high efficiency RGB QLEDs. These structures are similar to those proposed in [82]. The efficiency and emission spectra of the RGB QLEDs can be calculated by the dipole model [31, 96, 97] and the simulation results agree well with experiments. If we assume that quantum efficiency and the charge balance is unity, the corresponding EQE for the RGB QLEDs are 17.2%, 16.5% and 17.7%, respectively. These results are quite close to the reported experimental data. In addition, if we know the real quantum efficiency and charge balance of the device, we can get a better match between simulation and experiment. The calculated normalized emission spectra of the RGB QLEDs are shown in Figure 27 (b).

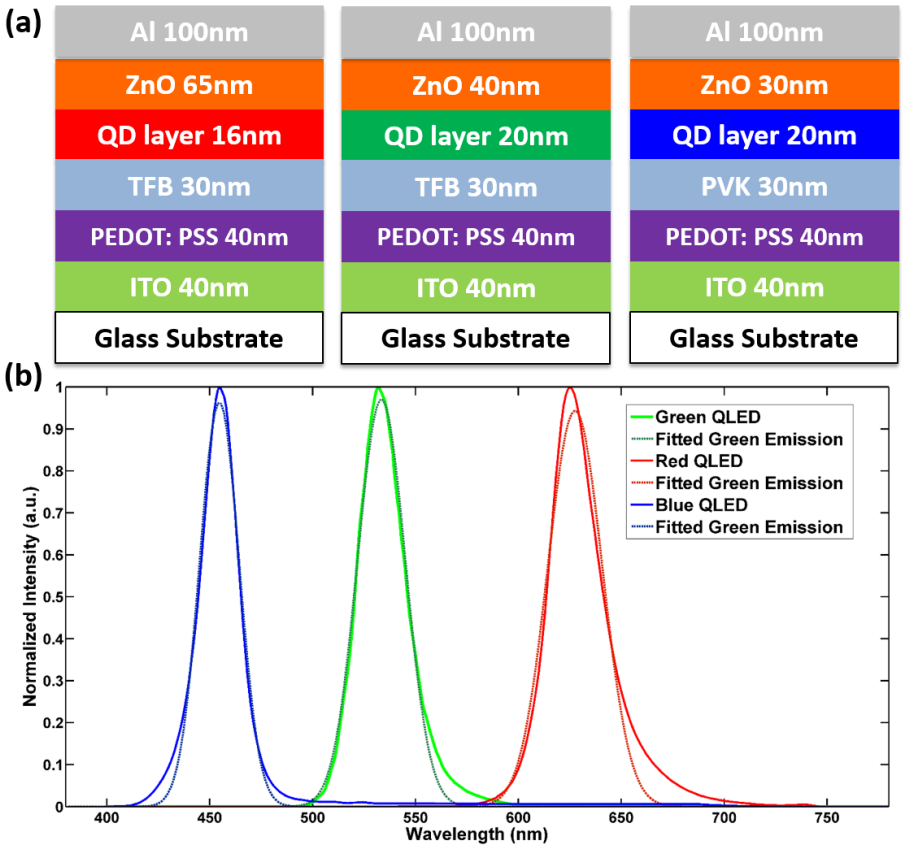

Figure 27: (a) Device structures and (b) emission spectra of the RGB QLEDs.

From Figure 27 (b) we find that the emission spectrum of each QLED fits well with the Gaussian distribution; the R^2 values for all three curves are all larger than 99.7%. Here the RGB QLEDs shown in Figure 27 can realize 85% of Rec. 2020, which is still insufficient. We can still optimize the color gamut coverage and *LER* simultaneously for the QLED. Results are shown in Figure 28. The linewidths of the RGB QLEDs are 1) 30nm for RGB (blue curve; lower limit), 2) 30nm for red and green, and 20nm for blue (green curve, intermediate case), and 3) 20nm for RGB (red curve; upper limit). As expected, the green curve lies between the red and the blue curves.

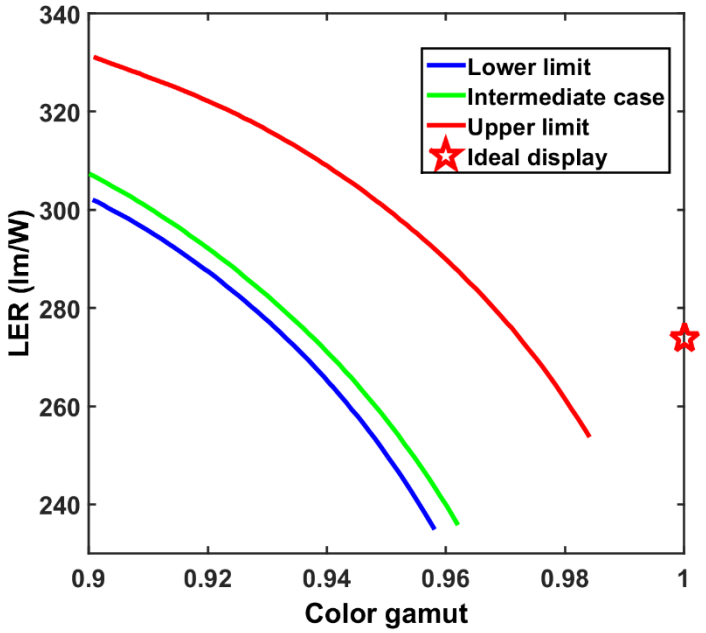

Figure 28: The relationship between color gamut and *LER* for RGB QLEDs.

From Figure 28, similar to QD-LCD, we cannot achieve 100% Rec. 2020 (ideal case) because of the linewidth of the RGB QLEDs. However, RGB QLEDs can easily achieve 95% of the Rec. 2020 standards even with a linewidth of 30nm because there is no crosstalk coming from color filters. If we compare the blue and red curves, we can easily find that at the same color gamut the *LER* is 13% higher for the QDs with 20nm linewidth. This suggests that for the EL case, developing QDs with a reasonably narrow linewidth (~20nm) is advantageous for both color gamut and efficiency. From Figure 28, we can find the following best result that RGB QLEDs can get: when the central wavelength of the 20nm-linewidth RGB QLEDs is 634.3nm, 530.6nm and 465.8nm, respectively, we can get an optimized 98.4% color gamut (99.0% in CIE 1976) with a high *LER* of 252.8 lm/W. Such a wide color gamut can be regarded as ready to reproduce most of the colors that Rec. 2020 enables [94]. Compared to the ideal display (100% Rec. 2020 color gamut with three monochromatic light sources), the *LER* of our RGB QLED is still 7.7% lower. If we

plot the color triangle in the CIE 1931 color space in Figure 29, we can easily catch that the red and blue colors are quite close to the Rec. 2020 color primaries while the green color is still a little bit off. Similar to QD-enhanced LCD, if we can squeeze the linewidth of the RGB QLEDs to 10nm, then we can realize 99.5% of the Rec. 2020 color gamut with *LER*=251.5 lm/W. However, it remains technically challenging to develop 10-nm-linewidth QDs.

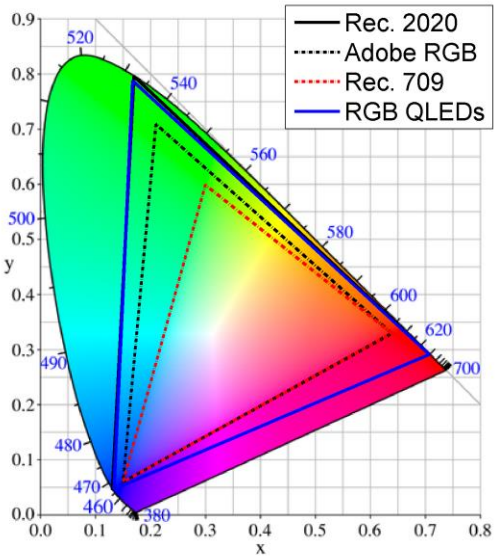

Figure 29: The Color gamut representation of the proposed RGB QLEDs.

4.4 Discussions

Before we dive into the discussions about quantum dots for Rec. 2020 color gamut. We would like to talk about some general concerns about wide color gamut displays. The first concern is about observer metamerism [98, 99]: namely, different observers will see the same color differently, especially for saturated colors. The other concern is that without proper color management, quite a few colors will appear strangely on a wide color gamut display, for example, skintone. While I agree that these concerns are reasonable, the hardware itself is not to blame. And

it is possible to mitigate these problems by multi-primary displays and better color management [98, 99]. It will be fun when the color scientists and hardware engineers work together to deal with these problems.

4.4.1 Color Space selection

As we have briefly mentioned before, the selection of color space for calculating color gamut is quite important but sometimes misleading. For example, considering the RGB QLEDs shown in Figure 27, the color gamuts in the CIE1931 and CIE1976 color space shown in Figure 30 (a)-(b) are 84.6% and 85.4%, respectively. The spectra of the RGB QLED are shown in Fig. Figure 30 (c) and the LER of the RGB QLED display is 290.8 lm/W. From Figure 30 (a)-(b), we can find that even though statistically speaking the color gamut in CIE 1931 and CIE 1976 is quite similar, the visual feeling is quite different. In Figure 30 (a), it seems that the QLEDs can well reproduce both red and blue, but not green. However, in CIE 1976 Chromaticity Diagram it seems that the QLED can better reproduce green than red and blue. To answer which representation is closer to reality, we convert the Rec. 2020 standard and the QLED color gamut to the CIELAB color space, and the results viewed down from the L axis is shown in Figure 30 (d). The wireframe color gamut is the Rec. 2020 standard and the solid color gamut is the color gamut of the QLED display, we can intuitively determine that the maximum mismatch happens in the green color. This suggests the color gamut shown in CIE 1931 color space is more correlated to the 3D color perspective model, which matches the conclusion stated in [24]. Under this consideration, we decide to calculate color gamut in CIE 1931. For real products, we have to analyze the color difference of the display quantitatively and further calculate the volume-coverage ratio.

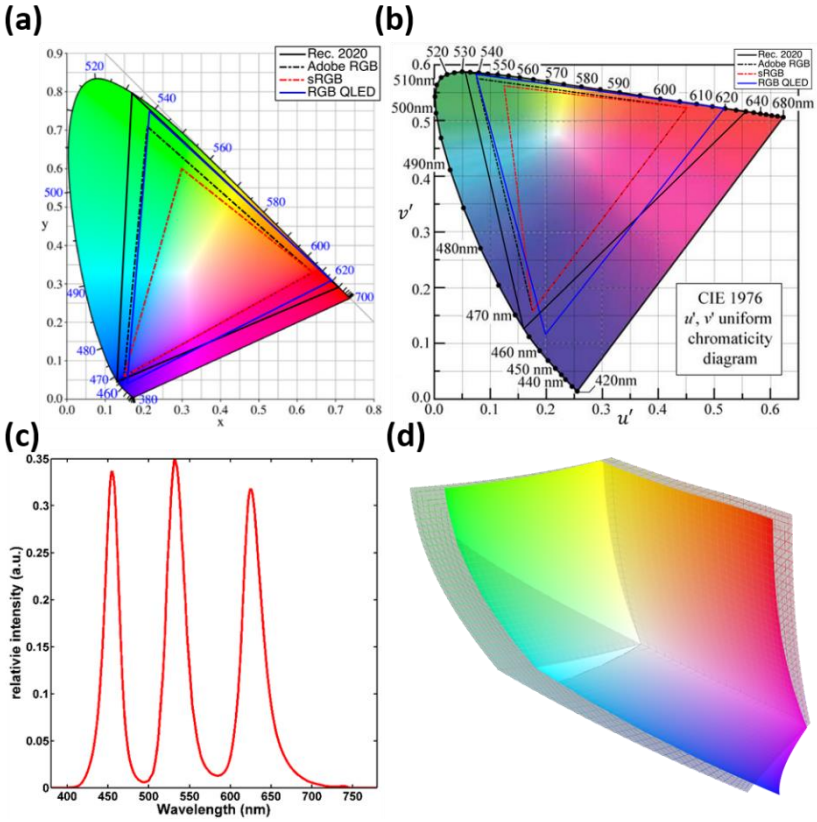

Figure 30: Color gamut of a RGB QLED in (a) CIE 1931 and (b) CIE 1976; (c) emission spectra of the RGB QLEDs and (d) color gamut comparison of Rec. 2020 and the QLED display in CIE LAB, the wireframe color gamut is Rec. 2020 and the solid color gamut is the RGB QLED.

4.4.2 Angular performance of QD-LCD and RGB QLEDs.

Color shift at an off-axis angle is a critical issue. For a QD-LCD, the angular performance is primarily determined by the birefringence of the LC material [100]. Here we demonstrate that with two wide-view LC modes: 1) two-domain (2D) n-FFS for smart phones and 2) 4D MVA for TVs. From Figure 31 (a)-(b), the color shift of each RGB primary color is rather small and the blue has the largest color shift. For the worst scenario, the color shift (Δu'v') of the blue color stays below 0.01 at 80° viewing angle. Such an LCD has negligible color shift. However, the color shift for the white color is much larger. For the 2D n-FFS mode, the color shift is still smaller than 0.02

at 80° for RGB and white. The situation for 4D MVA is drastically different. For the white color, the color shift is approaching 0.04 at 80° viewing angle. The small color shift for the RGB primaries means that we do not have to worry about the color gamut shrink at large viewing angle. While the small color shift for the white color in 2D n-FFS indicates that we can avoid the usage of color mixing films [101] The reason that 4D MVA has a larger color shift than 2D n-FFS is that for 4D MVA the LC directors are vertically tilted, while for 2D n-FFS the LC directors are rotated in plane. In the former case, it is easier to observe the birefringence effect at off-axis. In commercial TV products, 8D MVA is commonly used to mitigate the color shift [90].

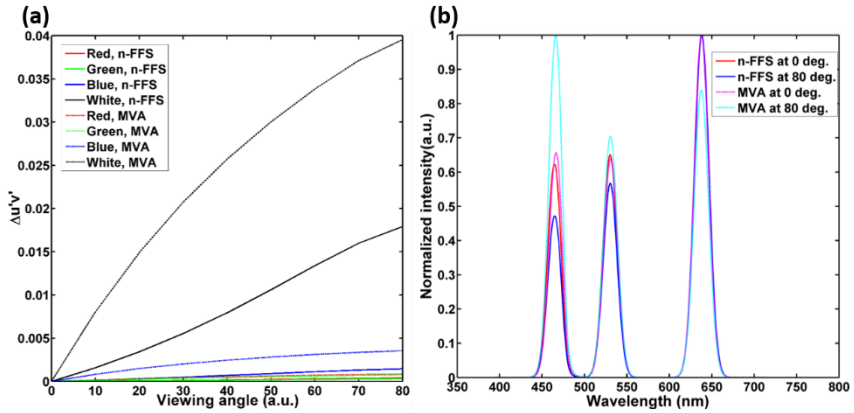

Figure 31: (a) Color shift of QD-LCDs for 2D n-FFS and 4D MVA, and (b) the normalized output spectra of the QD-LCD at different viewing angle.

As for the RGB QLEDs, color shift comes from cavity effect [102], The angular performance of RGB QLED can also be evaluated by the dipole model. For example, for the RGB QLED mentioned in Figure 27, the angular dependent emission spectra are shown in Figure 32 (a) and we can find that each individual spectrum remains quite narrow even at a large off-axis angle. From Figure 32 (b), the color shift of each individual color R, G and B is quite small. The largest color shift Δu'v' for blue is still smaller than 0.002, which is quite small. As for the combined

white color, Δu'v' reaches 0.02 at 65°. The reason for the relatively large color shift for the white color can be deduced from Equation (13) and Figure 32 (a). As demonstrated in Equation (13), the white color is optimized for the normal viewing angle. For the off-axis angle, the emission pattern drops differently for different colors, thus Equation (13) no longer matches the system's white point. To reduce color shift, we can optimize the QLED cavities to tune the angular emission pattern. However, this approach is quite unintuitive and it is difficult to predict how the angular emission pattern changes with different QLED stack configuration. Another way is to use optical diffusers, microstructures or other kinds of color mixing films to mitigate the color shift. This approach has been widely used in contemporary LCDs [101].

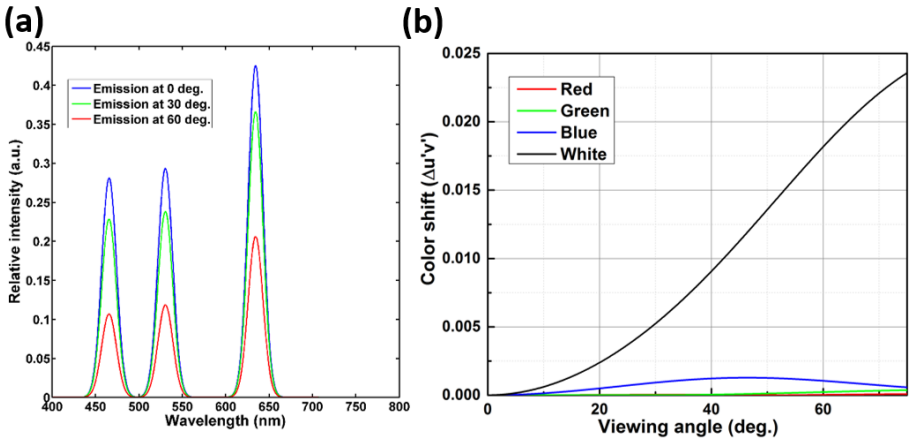

Figure 32: (a) Angular dependent emission spectra for the RGB QLED; and (b) Color Shift of the RGB QLEDs.

4.4.3 Comparing QD-LCD with red and green phosphors embedded LCD

Besides QDs, two-phosphor LEDs (2p-LED, i.e. blue LED pumping red and green phosphors) have also attracted much attention because of their excellent reliability and low cost. Figure 33 (a) shows the emission spectra of such a 2p-LED [77, 103]. From Figure 33 (a), the green and red emission spectra are relatively broad as compared to quantum dots. Our simulation

results in Figure 33 (b) show that for this 2p-LED backlit LCD system with the color filters designed for TV, it covers 90% of the Adobe RGB and 67% of the Rec. 2020, and the *TLE* is 21.7 lm/W for the n-FFS mode and 15.6 lm/W for the MVA mode. Therefore, we find that theoretically QD offers wider color gamut and higher optical efficiency than 2p-LED. However, contemporary red and green phosphors can be deposited on top of the blue LED chip to form a white LED [104]. whereas for red and green QDs, it is still not mature to place them on the blue LED chip [105] because of the material reliability issue. The "on edge" and "film" approaches for QDs are not as efficient as the white LED with 2p phosphors because of the longer optical path.

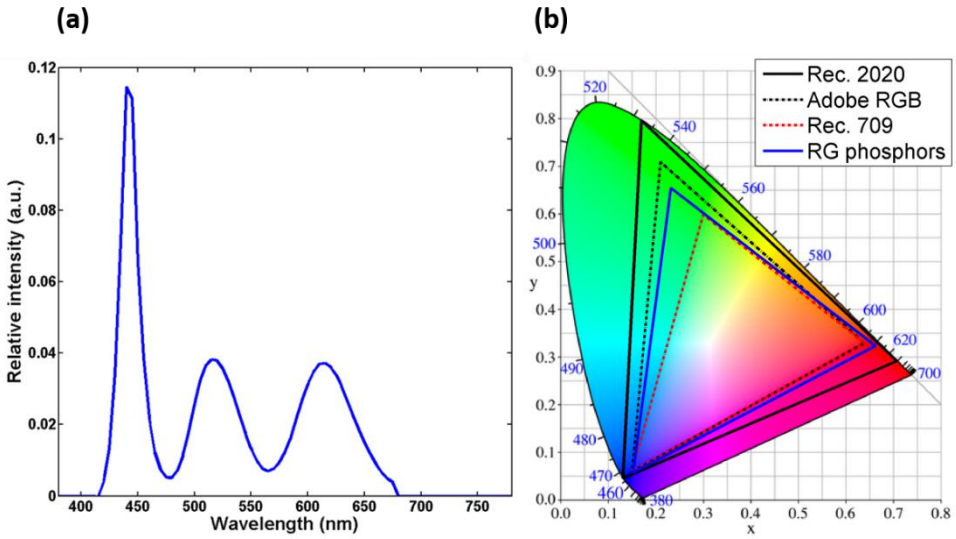

Figure 33: (a) The spectra of the RG phosphor embedded LCD and (b) its color triangle.

Recently, the red KSF phosphor [106] became the star for the display industry because of its deep saturated colors. Combining blue LED with red KSF phosphor and another green phosphor has become the standard approach for wide color gamut displays nowadays. While this configuration has no problem achieving the DCI-P3 color gamut, it is still inferior to QDs in terms of Rec. 2020, especially for the green color. At the same time, this new 2p-LED lacks the flexibility of the QD approach.

4.5 Summary

Wide color gamut is another import feature of HDR displays. We have analyzed how to obtain a wide color gamut display for both QD-LCD and RGB QLEDs. The relationship between optical efficiency and color gamut is explained for both approaches. For QD-LCDs, we can easily achieve more than 90% of the Rec. 2020 standard through spectral optimization with contemporary commercial color filters. However, to realize more than 97% of Rec. 2020, color filters have to be modified and TLE sacrificed. The angular performance of QD-LCDs is determined by the LC mode. With 2D n-FFS mode, the combined white color exhibits an indistinguishable color shift. As for RGB QLEDs, it can easily achieve Rec. 2020 through spectral optimization, and the angular performance of the QLEDs is mainly governed by the QLED cavity. For each primary color, the color shift is negligible; but for the combined white color, the color shift might still be noticeable. This knowledge can be used to design wide color gamut HDR displays.

CHAPTER FIVE: ACHIEVING 12-BIT PERCEPTUAL QUANTIZER CURVE FOR HIGH DYNAMIC RANGE DISPLAY

For HDR displays, we need more bit-depth to accommodate for the enlarged luminance range [18, 107]. Analysis of the human contrast sensitivity function indicates that the traditional 8-bit gamma encoding is no longer suitable for HDR content. Because of this, new electoral-optical transfer functions (EOTFs) have been proposed to replace the 8-bit gamma encoding. Among them, the most important ones are the hybrid log-gamma (HLG) encoding and the perceptual quantizer (PQ) curve [30]. The PQ encoding is also known as the ST.2084 standard. While both curves have been widely used, the HLG encoding is only intended for live production. Generally, it is believed that the 12-bit PQ curve covering 0-10,000 nits should be an ultimate goal for the display industry, as it guarantees no visual banding between adjacent grey levels.

Two display technologies could be implemented as HDR displays. The first one is OLED, which is possible to achieve perfect pitch black. However, because of the material lifetime concern, its peak brightness is usually below 1000 nits. The second approach is to use dimmable LED arrays as LCD backlight to dynamically control the dark state of the device. Currently, the peak brightness of LCD using local dimming backlight can achieve 4000 nits. With the emergence of high brightness LEDs, it is possible to achieve 10,000 nits in the near future. Therefore, achieving 12-bit PQ curve will become more and more critical for the display system. In this thesis, we will focus on the local dimming LCD approach. Finally, the author would like to mention that for cinema systems, there is a different criteria to be certificated as HDR. The main difference

5.1 Achieving 12-bit PQ curve: Driving the LC and LED separately

Figure 34 illustrates the 12-bit PQ curve together with a 12-bit gamma 2.2 curve. The detailed equation for describing the PQ curve can be found in [30]. From Figure 34 we can see that compared with the traditional gamma curve, the PQ curve increases much more slowly. In addition, there are ~2000 gray levels in the low luminance range (i.e. 0-100 nits). This ensures that the PQ curve is compatible with contemporary SDR standards. Assuming the peak brightness of the system is L and the contrast ratio of the LC panel is C, then the minimum brightness of the LCD without local dimming is L/C. This gives us an intuitive and straightforward driving method for the local dimming system:

1) For the luminance between L/C and L, the LED backlight is working at full brightness and we could control the LC panel to get the required luminance range.

2) For the luminance under L/C, the LC is turned to off state whereas the LED is dimmed to achieve the target luminance range.

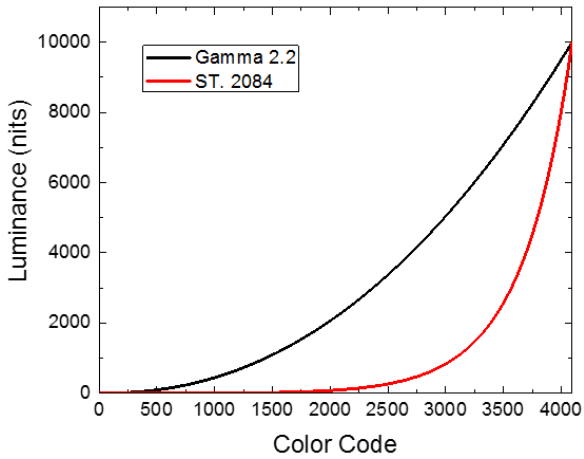

Figure 34: The 12-bit ST-2084 curve displayed together with the 12-bit gamma 2.2 curve.

Throughout this thesis, we assume the system peak brightness L is 10,000 nits. As for the LC part, we decide to use the vertical alignment (VA) mode [108] because of its high contrast ratio. Considering the capability of current TFT technology, we set the voltage interval between two adjacent gray level is around 5 mV, thus for a 12-bit display, the voltage swing ($\Delta V = V_{on} - V_{th}$) should be ~20 V. To achieve this ΔV, in experiment we mixed a negative dielectric anisotropy ($\Delta\varepsilon < 0$) LC material ZOC-7033 (JNC, Japan) [109] with a positive $\Delta\varepsilon$ LC material MLC-6686 (Merck). The recipes for the new LC mixture are listed in Table 5. The obtained new LC mixture exhibits a small, but negative dielectric anisotropy ($\Delta\varepsilon = -0.89$), thus a large voltage swing (ΔV ~20 V) can be achieved.

Table 5: Recipe for the new LC mixture.

Component	**ratio**	**Δn**	**Δε**
ZOC-7003	75.2%	0.103	-4.36
MLC-6686	24.8%	0.0983	10.00

Next, we filled this new LC mixture into a commercial VA test cell with cell gap $d = 3.3\mu m$. Figure 35 shows the measured voltage-transmittance (VT) curve of the mixture, in which the threshold voltage V_{th} is 11.12V and on-state voltage $V_{on}\approx 30V$. The measured contrast ratio of the LC cell is ~5000:1. This indicates that driving the LC alone we can get 2 nits to 10000 nits; below 2 nits we need to dim the LEDs to achieve the target luminance.

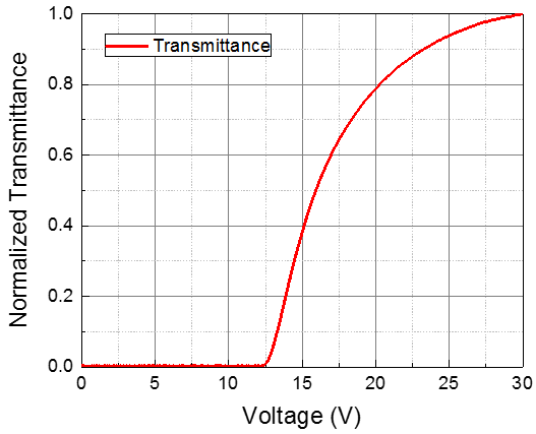

Figure 35: Measured VT curve of the LC cell: d=3.3 μm and λ=633 nm.

To analyze the performance of the LC cell, we selected 24 gray levels based on the 12-bit PQ-curve. The 24 gray levels are listed in Table 6.

Table 6: The selected 24 gray levels.

Gray level	**Luminance (nits)**	**Corresponding transmittance (%)**	**Gray level**	**Luminance (nits)**	**Corresponding transmittance (%)**
771	2.002	0.020	2303	170.274	1.703
865	2.904	0.029	2462	246.848	2.468
965	4.197	0.042	2623	357.454	3.575
1073	6.090	0.061	2785	516.542	5.165
1187	8.817	0.088	2950	749.196	7.492
1307	12.747	0.127	3115	1084.617	10.846
1434	18.473	0.185	3280	1569.166	15.692
1566	26.705	0.267	3446	2276.360	22.764
1705	38.762	0.388	3610	3292.626	32.926
1848	56.101	0.561	3773	4764.176	47.642
1996	81.278	0.813	3935	6902.473	69.025
2148	117.722	1.177	4095	10000.000	100.000

As discussed above, ~50% gray levels are in the low luminance region. For such a low transmittance, the driving voltage would be quite close to the threshold voltage; therefore, the response time would be slow [110]. To confirm this, we measured the gray-to-gray (GTG) response time between these twenty-four gray levels, and results are tabulated in Table 7. The average GTG rise time of the LC cell is 33 ms, which is too sluggish for practical applications. This indicates driving the LC and the LED separately is not suitable for the 12-bit display.

Table 7: The gray-to-gray response time of the LC cell between the selected 24 gray levels. (Unit: ms)

	1	**2**	**3**	**4**	**5**	**6**	**7**	**8**	**9**	**10**	**11**	**12**	**13**	**14**	**15**	**16**	**17**	**18**	**19**	**20**	**21**	**22**	**23**	**24**
1		123.6	120.8	116.4	111.7	106.3	93.0	89.1	83.1	79.2	72.3	66.2	60.3	54.1	40.3	39.7	36.1	32.4	29.3	26.9	17.4	13.0	8.0	2.5
2	2.5		105.0	96.6	86.0	76.4	76.2	72.5	68.8	67.4	62.4	58.2	52.6	48.9	43.7	38.6	32.7	29.1	25.0	20.3	15.7	11.8	7.7	2.4
3	2.6	88.8		95.8	89.4	85.2	79.8	75.0	71.3	66.4	62.6	58.3	53.4	49.1	41.9	38.8	35.1	28.9	23.9	19.6	15.7	11.6	7.7	2.4
4	2.6	85.8	95.2		78.7	76.0	74.3	74.1	69.6	67.8	62.8	58.8	54.1	49.2	41.4	40.9	32.6	28.6	24.5	19.8	15.7	11.6	7.6	2.4
5	2.6	83.2	76.0	84.6		76.8	74.4	72.1	70.6	69.1	64.2	58.0	53.0	48.2	41.6	40.3	32.9	28.4	24.2	19.8	15.4	11.5	7.5	2.4
6	2.6	80.2	78.4	80.2	80.3		73.8	68.4	67.7	66.6	60.5	57.3	52.3	48.1	41.0	37.5	35.4	28.2	23.9	19.3	15.5	11.4	7.5	2.4
7	2.7	73.1	71.7	75.3	70.7	71.9		67.8	61.2	60.3	59.4	54.0	49.8	47.2	40.1	35.0	33.7	28.2	23.2	19.6	15.3	11.6	7.6	2.4
8	2.7	68.5	69.5	73.0	70.3	71.9	66.0		63.0	60.0	57.6	53.7	48.8	45.1	40.6	34.7	33.1	28.5	22.3	18.8	14.7	11.3	7.4	2.4
9	2.8	66.3	67.4	68.6	68.6	68.2	61.1	59.3		58.2	55.3	50.8	48.0	43.8	40.0	36.7	31.3	26.5	23.0	18.4	14.9	11.1	7.4	2.4
10	2.8	62.7	64.0	63.8	63.8	63.3	60.2	58.7	57.1		54.2	50.8	47.0	42.7	40.6	37.0	31.0	26.7	22.1	18.2	14.5	11.0	7.3	2.3
11	2.8	58.4	59.2	58.5	57.9	58.0	57.1	55.4	56.7	57.3		48.6	43.8	40.2	34.1	33.7	28.8	25.7	22.3	17.5	14.4	10.9	7.1	2.3
12	2.9	54.7	54.8	55.2	55.8	54.6	52.1	52.1	51.6	48.4	49.7		42.0	39.7	35.9	33.1	29.9	25.9	21.5	18.0	14.3	10.6	7.1	2.3
13	2.8	50.1	51.1	50.7	50.5	50.5	49.3	47.6	47.5	45.4	43.9	42.5		39.0	32.3	30.4	26.2	23.6	21.1	17.3	13.6	10.4	6.9	2.2
14	2.9	46.1	46.5	46.5	46.4	46.0	45.9	44.6	44.0	43.4	42.2	41.6	38.1		32.2	33.7	26.3	24.4	19.7	17.0	13.8	10.3	6.8	2.2
15	3.0	43.4	39.2	42.2	41.5	42.2	45.2	44.0	44.3	38.6	39.6	39.4	39.3	34.9		31.7	27.9	22.8	19.2	16.2	13.4	9.9	6.6	2.2
16	3.1	39.4	37.2	40.6	40.2	37.3	37.2	39.5	38.2	37.9	35.7	32.5	31.4	33.0	28.0		27.0	21.7	19.5	15.6	12.5	9.9	6.5	2.2
17	3.2	35.7	36.9	35.2	33.5	36.5	36.2	38.5	37.2	33.9	32.2	32.5	29.3	30.7	26.9	29.0		24.4	17.4	15.4	12.7	9.3	6.3	2.1
18	3.4	33.5	31.4	31.3	31.2	31.1	31.6	34.2	33.0	30.8	30.0	31.1	30.5	29.0	26.5	23.7	21.8		18.2	14.8	12.2	9.1	6.2	2.1
19	3.6	30.2	27.8	29.3	29.0	29.2	28.7	27.9	29.1	27.6	28.7	27.8	26.0	25.9	25.3	24.2	21.2	19.2		15.6	12.0	8.7	6.2	2.0
20	3.7	25.9	25.5	27.0	26.9	26.5	26.0	27.3	27.3	26.0	25.4	26.0	24.1	24.4	23.0	21.6	20.2	19.0	16.6		10.8	8.6	5.7	2.0
21	3.9	23.8	23.1	24.1	24.1	23.9	23.9	23.3	24.6	23.8	23.2	23.8	23.0	22.7	21.3	20.5	19.2	16.6	15.6	14.2		8.7	5.8	1.9
22	4.1	20.7	20.9	21.8	21.8	21.5	21.5	22.1	21.7	21.7	22.2	21.9	21.9	21.2	19.7	19.1	17.8	16.2	14.8	12.9	10.4		5.8	1.9
23	4.4	18.2	19.0	19.7	19.7	19.6	20.1	20.3	20.2	20.4	20.2	20.4	20.3	19.8	19.2	18.1	17.2	15.5	13.9	12.1	10.2	8.0		1.7
24	4.9	16.5	17.0	17.3	17.5	17.3	17.9	17.9	18.1	18.2	18.1	18.1	18.1	17.9	17.7	16.6	16.2	14.8	13.4	11.6	9.8	7.9	5.5	

5.2 Achieving 12-bit PQ curve: Driving the LC and LED simultaneously

As analyzed above, driving the LC panel or the backlight LEDs alone is not suitable for achieving the 12-bit PQ curve. Thus, we need to drive the LC and the LEDs simultaneously. The most intuitive approach can be explained by Equation (15):

$$L(G_1, G_2) = L(G_1)T(G_2). \tag{15}$$

Here, G_1 and G_2 represent the gray level of the LED and the LC, respectively, L is the luminance of the system, and T is the transmittance of the LC. By controlling the gray level of the LC and the LED simultaneously, it is possible to achieve 12-bit PQ curve. Assuming the LEDs and the LC panel have S_1 and S_2 gray levels, respectively, in theory the system will have $S_1 \times S_2$ gray levels. An example is that the LEDs are 4-bits (16 gray levels) and the LC panel is 8-bit (256 gray levels).

The abovementioned approach is quite straightforward; however, a severe flaw of this approach is that the same luminance may be achieved by different gray level combinations. This reduces the overall gray levels of the system. At the same time, without careful gray level selection, this approach will introduce severe image noises. This can be explained by the following thought experiment: the display is required to show two adjacent achromatic pixels and the target luminance for the two pixels are 100 and 93.88 nits, respectively. Assuming the LC panel follows the 8-bit gamma 2.2 curve, at least two possible gray level combinations can achieve the targets:

1) For both pixels, the LEDs work at 100 nits, and the LC works at gray level 255 for the first pixel and gray level 248 for the second pixel. The actual luminance for the two pixels are 100 and 94.06 nits, respectively.

2) For the first pixel, the LED works at 100 nits and the LC works at gray level 255; for the second pixel, the LED works at 1000 nits whereas the LC works at gray level 87. The actual luminance for the two pixels are 100 nits and 93.88 nits, respectively.

At first glance, the two combinations seem identical and the second combinations seems even closer to the target luminance. However, in real applications the first combination is superior to the second one. The first reason is that in local dimming LCDs, most of the time it is not possible to do pixelated local dimming [1, 19, 49], thus, the two pixels might belong to the same section where only one LED is available. The second reason is that even if it is possible to do pixelated local dimming, because of the point spread effect [1], there will be crosstalk between the adjacent pixels, and the second configuration will introduce salt-and-pepper noises [111] to the displayed image. In this sense, a driving scheme where there is no sudden jump in gray level combinations is preferred. Based on this requirement, we propose a new driving scheme with the following steps:

1) Predetermine a tone response curve L_i of the LEDs, here L is the luminance and i=0, 1, 2,.., N_1-1 is the (i+1)-th gray level. In total, there are N_1 grey levels.

2) For the target luminance L_t that satisfies $L_i \leq L_t < L_{i+1}$, the gray level of the LED for this target is set to i+1.

3) Determine the corresponding LC transmittance T_j based on Equation (15). After calculating all the LC transmittance for all the target luminance, it becomes possible to construct the tone response curve T_j of the LC panel. Here j is the (j+1)-th gray level of the LC panel. In total there are N_2 gray levels.

4) Optimizing the tone response curve L_i and T_j according to the device limit and the 12-bit PQ curve.

With the abovementioned approach, we can ensure that one target luminance corresponds to a single gray level combination, and the gray level combinations will change smoothly if properly designed. Based on this approach, we designed the tone response curve of the LEDs and the LC by comparing with the 12-bit PQ curve. The tone response curves for the LEDs and the LC are shown in Figure 36 (a)-(b), respectively. Here we have 57 gray levels for the LEDs and 256 gray levels for the LC. When they are combined together, the final tone response curve is shown in Figure 36 (c) and it is clear that this curve matches well with the 12-bit PQ curve.

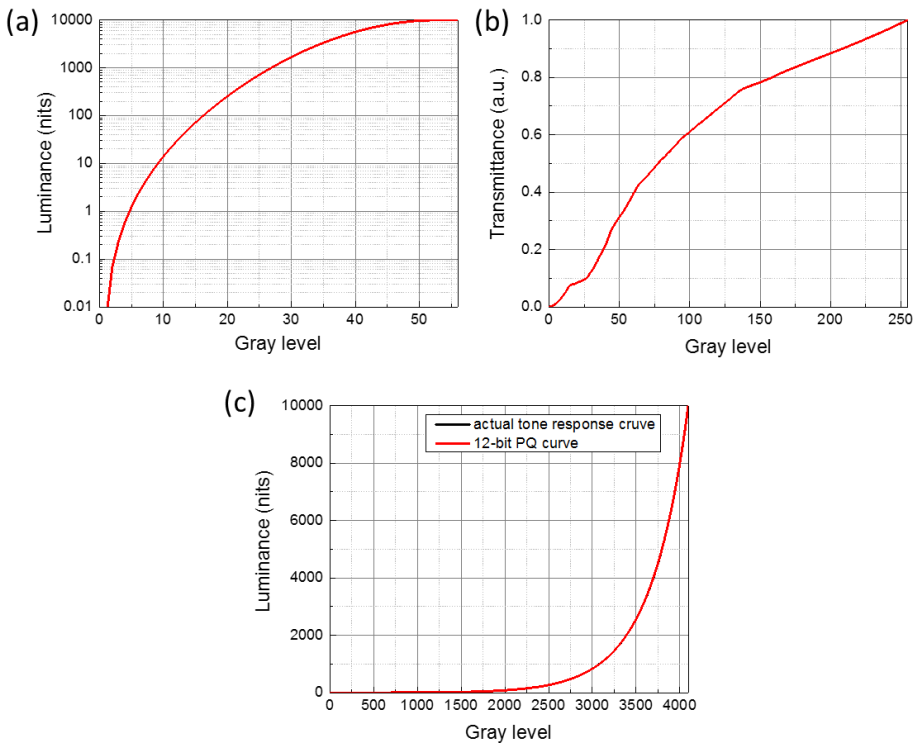

Figure 36: Tone response curves of (a) the LEDs, (b) the LC panel and (c) the whole system in comparison with the target 12-bit PQ curve.

To quantify the difference between the actual tone response curve *M* and the 12-bit PQ curve *R*, we calculated the coefficient of variation (CV) [112] between the two curves, and the definition of CV is:

$$CV = \frac{100\%}{\overline{R}} \sqrt{\frac{\sum_{0}^{N-1} (M_i - R_i)^2}{N}}. \tag{16}$$

Here N is the total gray levels and $\overline{R}$ is the average luminance of the PQ curve. As can be seen from Equation (16), the CV describes the agreement between the two data sets. The calculated CV here is 0.08%, which indicates with our proposed tone response curves shown in Figure 36, the system can well reproduce the 12-bit PQ curve.

In the previous section, we have mentioned that if we drive the LEDs or the LC separately, the LC panel will have sluggish response time and high on state voltage. For our driving scheme proposed above, the response time and driving voltage of the LC panel is no longer a problem as the panel is still 8-bit except that the tone response curve is different. To prove this, we made a 3.3μm-cell-gap VA cell with ZOC-7003. The V-T curve of the cell is shown in Figure 37. The on-stage voltage of the cell is 7.5V with a threshold voltage of 2.25V. Such driving voltage is typical for commercial LCD systems.

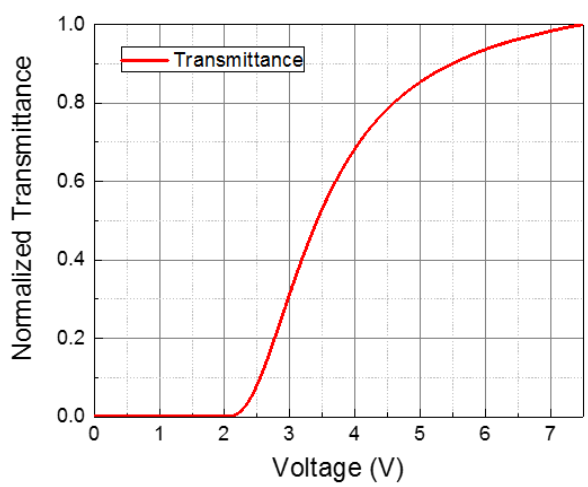

Figure 37: The voltage-transmittance curve of VA cell using ZOC-7003.

As for the response time, the transmittance curve is equally divided into 8 gray levels and the measured GTG response times [63, 64] are shown in Table 8. The average response time of the cell is 6.17 ms. Such response time is fast enough for real applications.

Table 8: Gray-to-gray (GTG) response time of the ZOC-7003 VA cell. (ms)

Gray levels	**1**	**2**	**3**	**4**	**5**	**6**	**7**	**8**
1		17.01	12.51	10.01	8.2	6.04	3.07	1.1
2	2.85		11.25	9.19	7.07	4.87	2.82	0.97
3	3.34	12.15		8.3	6.43	4.66	2.64	0.88
4	3.65	11.82	9.61		6.09	4.39	2.51	0.83
5	3.97	11.39	9.46	8.45		4.44	2.41	0.8
6	4.31	11.04	9.41	7.81	6.19		2.4	0.79
7	4.71	10.44	9.3	7.79	6.17	4.58		0.69
8	5.15	10.55	8.96	7.51	5.86	4.21	2.2	

5.3 Summary

We have proposed an approach that drives the local dimming LED backlight and LC panel simultaneously to achieve the 12-bit PQ curve for HDR displays. Compared to driving the LEDs and LC panel separately, this approach exhibits fast response time and acceptable driving voltages. At the same time, our approach will not introduce imaging noise to the system.

Besides driving the LEDs and the LC panel together, another possible way to achieve the 12-bit PQ curve is to use the dual LC panel approach, which we have already talked about in Chapter 2. In this approach two LC panels are driven together to achieve increased bit-depth and darker black state. One common difficulty for these two approaches is the synchronization: for the first approach, the synchronization between the LEDs and the LC will be the main challenge whereas for the second approach synchronizing the two LC panels will be a burden for the circuit design. Besides this challenge, each approach has its unique pros and cons. For the first approach, designing the LED backlight will be quite challenging, as we have to consider the point spread function of the LEDs, also, the backlight design will be even more complex if we would like to use edge-lit LEDs instead of direct-lit LEDs [113]. For the second approach, the added LC panel reduces the overall optical efficiency and increases the thickness of the system. In the author's opinion, these two approaches would co-exist for different requirements and user scenarios.

CHAPTER SIX: REPRODUCING HIGH DYNAMIC RANGE CONTENTS BASED ON DISPLAY SPECIFICATIONS

As we have mentioned in the introductory chapter, besides the hardware limit, current display pipelines treat the HDR contents incorrectly, which result in image rendering that violates the content creator's intension. At the same type, because of the manufacturing tolerances, even the same batch of displays might have different white point, peak brightness and dark state. That is why we want to improve the display pipelines to reproduce the HDR contents adaptively based on display configurations.

Before we dive into the topic, we would like to mention that there are two kinds of HDR content: HDR images and HDR videos. The difference between these two are that most of the time HDR images do not come with absolute luminance info whereas professional color graded HDR videos contain absolute luminance info via the PQ encoding. In our analysis, we will only talk about professionally graded HDR video footage.

6.1 Reproducing HDR content via HDR gamut mapping

As is mentioned above, standard display pipeline cannot faithfully reproduce HDR content. Displaying HDR content on all kinds of media is actually not new topic and there are many tone mapping approaches around to deal with this problem, for example, the iCAM06 image appearance model [16] and the photographic tone mapping approach [114]. These algorithms work quite well in terms of HDR imaging. However, they are not suitable for displaying HDR videos in real time: the fast-bilateral spatial filtering used in iCAM06 consumes too much processing power. In the photographic tone mapping approach, calculating the average luminance of each frame is quite challenging if we would like to display 4K HDR video in real time. In this sense, a color-by-color

solution is preferred as it can be constructed as a color look up table (CLUT) and incorporated into silicon, such as the graphics hardware or the display timing controller. This motivates us to develop a new color-by-color reproduction approach to display HDR content. Before we talk about our approach, we would like to look at how contemporary TVs interpret HDR content, which is shown in Figure 38 (a). After decoding the content to RGB values, the contents are first gamut mapped and then tone mapped [115] before finally being displayed on HDR/SDR display. For content encoded with Dolby Vision, this process can be done with the dynamic metadata [116]. However, for content encoded with HDR10, this process is dependent on the TV manufactures. In our approach, we combine the two processes together by manipulating the lightness and chroma simultaneously through HDR gamut mapping, as is demonstrated in Figure 38 (b).

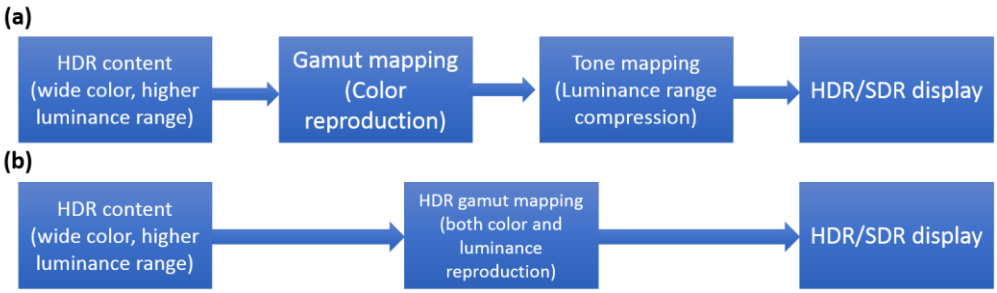

Figure 38: (a) Display pipeline for HDR contents on contemporary TV and (b) the proposed HDR gamut mapping algorithm.

The detailed approach of the HDR gamut mapping is explained below:

1) Determine the reference white. The reference white we select has absolute XYZ value of (76.0374, 80.0000, 87.1176). This white point is selected based on the content metadata, sRGB standard [117] and the fact that most displays have D65 white point. We'll talk more about reference white selection in the discussion part.

2) Select the working color space. Here we select the IPT color space [118] because of its simplicity and hue linearity. The IPT color space is extended to beyond unity to allow for RGB values larger than one.

3) Construct the color gamut of an ideal wide color gamut HDR display. Here we assume the original display is an HDR display with a peak brightness of 1200 nits and is fully capable of displaying BT. 2020. All the colors it can reproduce is converted to the IPT color space. Color space selection will be explained in more details later in this chapter.

4) Construct the color gamut of the real SDR display. The target display here is with peak brightness of 400 nits and sRGB color gamut. Similarly, all the colors it can reproduce is converted to the extended IPT color space.

5) Gamut mapping from the original color gamut to the destination color gamut. The approach we use here will be explained later. Of course, content creators can opt for other gamut mapping approaches.

6) Transform the gamut-mapped content back to display RGBs.

The color gamut of both the HDR and the SDR display is demonstrated in Figure 39 (a) and the general working principle of the HDR gamut mapping approach is depicted in Figure 39 (b). Basically this approach scales lightness and chroma on a constant hue plane. The advantages of this approach are threefold: 1) This color-by-color reproduction approach is relatively easy to incorporate it into the hardware level as a 3D CLUT; 2) This approach is display adaptive. For example, if the peak brightness of the SDR display is 600 nits, we just need to reconstruct the destination color gamut, do gamut mapping again and create another 3D CLUT; 3) it is flexible enough to incorporate color preference.

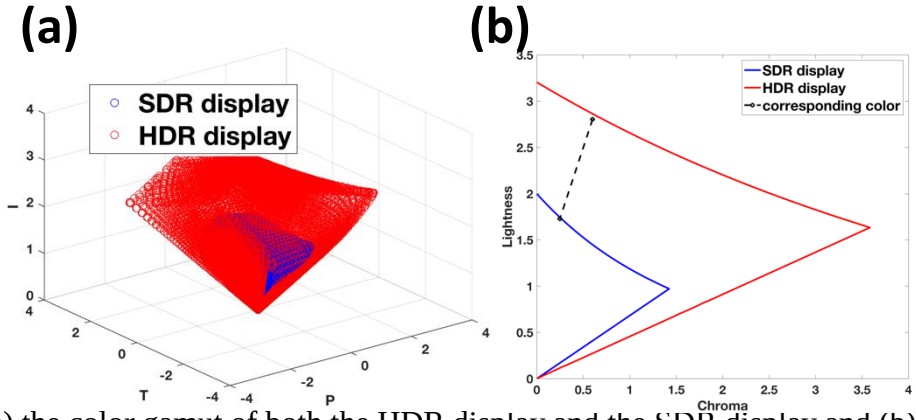

Figure 39: (a) the color gamut of both the HDR display and the SDR display and (b) the principle of the HDR gamut mapping approach.

The first step of the gamut mapping approach is the lightness mapping. The lightness mapping curve is shown in Figure 40. Here we use I_o and I_t to denote the peak lightness value of the original display gamut and the target display gamut, respectively. The mapping curve is designed based on these two principles: 1. For lightness values between 0 to 1, which corresponds to luminance between 0 and 80 nits, there is no lightness distortion. In this way contents with luminance level up to the reference white can be well preserved. 2. For lightness values larger than unity, they are mapped through a Bézier curve with control points (1,1), (I_o,I_o) and (I_t, I_o). With this step the highlights can be well preserved on the target display.

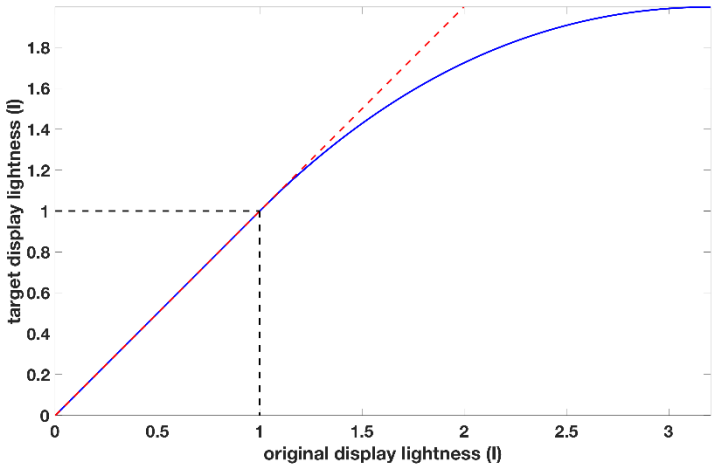

Figure 40: lightness mapping curve used in our algorithm.

The second step of the algorithm is the chroma mapping along constant lightness. This step is well documented in the BasicPhoto algorithm developed by Microsoft, which is a variant of the chroma-dependent sigmoidal lightness mapping and cusp knee scaling (SGCK) approach [119]. However, for our gamut mapping approach we are using the IPT color space.

6.2 HDR display setup

To test the algorithm, we built an HDR display by combining a projector with an LC module [18]. In this way we have formed a pixelated local dimming HDR display. The specifications of the HDR display are listed in Table 9. With this HDR display it is possible to both display HDR contents and simulate an SDR display.

Table 9: Specification of the HDR display.

Peak brightness	1160 nits
Dark State	0.002 nits
Contrast Ratio	580,000:1
Color gamut	sRGB
Bit depth	12 bit

The device model of this dislpay can be described by the following equation [120]:

$$\begin{bmatrix} X \\ Y \\ Z \end{bmatrix} = P(S)M(S)\begin{bmatrix} R \\ G \\ B \\ 1 \end{bmatrix} = P(S)\begin{bmatrix} X_R(S) & X_G(S) & X_B(S) & X_K(S) \\ Y_R(S) & Y_G(S) & Y_B(S) & Y_K(S) \\ Z_R(S) & Z_G(S) & Z_B(S) & Z_K(S) \end{bmatrix}\begin{bmatrix} R \\ G \\ B \\ 1 \end{bmatrix}. \quad (16)$$

Here S is the digital counts of the projector and P(S) describes the luminance attenuation of the projector, the matrix M transforms linear RGB values to CIE XYZ values by taking into consideration the light leakage of the panel. Note that M is also dependent on L because of the primary shift [121] of the projector under low light level. With Equation (16), when we get the XYZ value of the scene, it is possible to calculate a grayscale image for the projector and a color image for the LC module, and when they superimpose together we are able to reconstruct the original HDR scene. This process is demonstrated in Figure 41. This HDR image is from Dr. Mark Fairchild's HDR survey [2]. The gray level image and the color image are the actual image we sent to the projector and the LC module respectively, whereas the final image is a tone mapped version of the image through the iCAM06 image appearance model. Notice that this image is only used as a demo, it is not used in our pschophysical experiment. At the same time, this photo is different from common HDR images that this is a professional HDR image with absolute

luminance info. At the same time, this image is different from HDR videos that it uses a linear encoding and does not specify its color gamut.

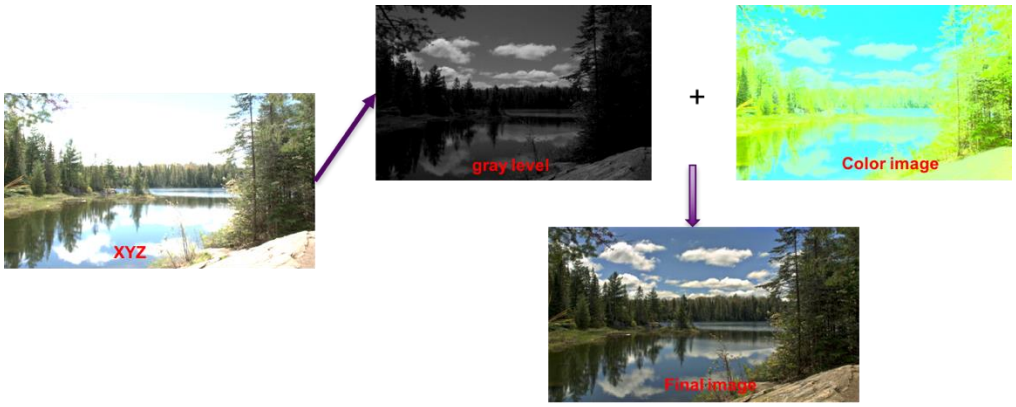

Figure 41: How HDR image is displayed on our HDR device.

6.3 The psychophysical experiment

Besides testing the algorithm, another reason we would like to set up this device is that even though contemporary SDR displays are still inferior to the HDR displays, it is possible to improve their performance to some extent. For example, the peak brightness of the SDR displays can be improved by using high efficiency OLED panel/LED backlight. Thus we would like to know how peak brightness and dark level will affect the performance of SDR display. For these two purposes, we conducted a psychophysical experiment. The experiment was conducted as follows:

We prepared eight HDR images and these images are listed in Fig. 8. The second image is the same as Figure 4 whereas all the other HDR contents are from the HDR clip *Colors of the Journey* and the images shown in Figure 42 are tone mapped versions of the original HDR frames via highlight compression. For each HDR image, ten versions were created: The first version was a gamut-mapped version from BT. 2020 to sRGB to accommodate the HDR display's color gamut, this version was still HDR. For the other nine versions, they were the SDR versions that had been

processed with the HDR gamut mapping. The difference between these images were that they came with three different peak brightness settings: 400 nits, 640 nits and 800 nits. As for the dark level, there were also three configurations:0.005 nits, 0.1 nits and 0.25 nits. Thus there were 10 versions in total. The psychophysical experiment was conducted through pair-wise comparison. A randomly selected version from the set of the SDR images was displayed together with the HDR image, and the viewers were asked to judge how similar these two images were based on five categories: 1) overall brightness 2) details 3) colors 4) highlights and 5) dark shadows. Then they gave a score between 0% (totally different) to 100% (identical) to describe the similarity between the two images. The viewing condition was dark with ambient illuminance of 10 lux.

Figure 42: The eight HDR frames we have used in the psychophysical experiment; these images are ton-mapped version of the original HDR scene.

This process is demonstrated in Figure 43. The top image is an SDR version with peak brightness of 400 nits and dark level of 0.25 nits while the bottom image is the HDR version. Figure 43 is taken directly from the HDR display and because of the camera limit, it is not identical to what the viewers saw on the display. Still we can tell that the HDR version has brighter highlights and better color saturation than the SDR version. However, comparing Figure 43 with Figure 4 we can tell that our HDR gamut mapping approach can well reproduce the HDR content.

Figure 43: Comparing the SDR image with the HDR version.

After all 18 viewers gave their answers for all of the images, we analyzed the data and found some important results. The first question we would like to ask is "black or white: which is more important?" The reason we ask this question is that the two mainstream display technologies have different challenges when dealing with HDR contents. For OLED the dark level can be perfectly black, but because of the lifetime issue it is not recommended to make the peak luminance too bright. On the other hand, for LCD the peak brightness can be extremely high by using high power LEDs, whereas the dark state is usually not satisfying because of the light leakage. The first conclusion is that dark level is as important as peak brightness. This can be seen from the results for Figure 42, image (2) and (3), which is listed in Table 10. Here b stands for dark level and w stands for peak brightness. For image 2 the average luminance of the scene is 220 nits and the sun area is over 1000 nits. When we increase the peak brightness, the perceived similarity between the SDR and the HDR image dramatically increased, whereas when we decrease the dark level, the similarity did not improve much. In fact, if we calculate the correlation coefficient r_b between dark level and similarity score, the result is r_b=-0.159, which indicates poor correlation. Whereas for the relationship between peak brightness and similarity score, the correlation coefficient r_w=0.954. This indicates that for image (2), people care much more about the white level than the dark level.

As for image (3), the average luminance is only 0.38 nits and the night sky is intended to be pitch black. This time in general decreasing the black level has greatly improved the similarity score (r_b=-0.886), whereas the peak brightness is poorly correlated with the image similarity with r_w=-0.024. This indicates for this image, even though the stars should be over 1000 nits, people are much more sensitive to the black level because it is a night scene. For the other six images, the trend is similar: when highlights dominate the image, the similarity scores are well correlated with the peak brightness (Figure 42 (8)); and when the image is dominated by dark pixels, the similarity is most determined by the lowest dark level (Figure 42 (1)). For the other four images, the similarity is dependent on both the peak brightness and the dark level. Summarizing these results together, we can see the influence of peak brightness and dark level is image dependent and to cater to the entire different image types, the dark level and peak brightness should be improved simultaneously.

Table 10: Similarity (in percentage) for Figure 42, image (2) (data on the left side) and (3) (data on the right side).

b\w	**400**	**640**	**800**		**b\w**	**400**	**640**	**800**
0.005	55	61.31	68.13		**0.005**	67.81	72.63	70.19
0.1	56.25	61.44	63.63		**0.1**	70.88	70.31	69.63
0.25	52.19	61.19	65.31		**0.25**	60.63	60.81	57.88

When we look at the mean opinion score (MOS) for all the eight images, what we got is listed in Table 11, from the table we can see that for the worst scenario, viewers still give a high similarity score of 68.82%, which indicates our HDR gamut mapping approach works quite well. A closer look at the data demonstrates that in general higher peak brightness and darker black level improves the similarity. However, at 0.1 nits to 640 nits, people give a high similarity score of 75.05%, and the improvement after that is not that dramatic. From Table 11 we can tell that even though it is not possible for an SDR display to look 100% like an HDR display. Improved peak

brightness and dark level, together with our HDR gamut-mapping algorithm, helps enabling better viewing experience. At the same time, the viewing experience improvement is limited. Overall speaking, when we reduce the dark level from 0.25 nits to 0.1 nits, there is a noticeable improvement in similarity, however, when the dark level is reduced further to 0.005 nits, it is quite challenging for the viewers to notice the improvement. This suggests that 0.1 nits can be regarded as a minimum requirement for faithfully reproduce HDR content on an SDR display. As for the peak brightness, the improvement from 400 nits to 640 nits results in a boost in similarity score, whereas further boost the peak brightness to 800 nits can only mildly improvement the similarity. This indicates that compared with the HDR display with peak brightness of 1160 nits, 400 nits peak brightness is too "dim" and could not enable a visually appealing highlights representation. Whereas the boost from 640 to 800 nits is not significant enough to make the latter more similar to the original HDR scene. In the meantime, it is quite challenging to make an SDR display with 800 nits because of the high power consumption. These two reasons together suggest that 640 nits can be regarded as another minimum requirement for an SDR display to faithfully represent the HDR content. In summary, luminance range between 0.1 nits to 640 nits can be regarded as the minimum range for displays to appear HDR-like.

Table 11 Mean opinion similarity score (in percentage). (in percentage)

b\w	**400**	**640**	**800**
0.005	**71.92**	**75.92**	**76.70**
0.1	**72.41**	**75.05**	**76.98**
0.25	**68.82**	**73.98**	**75.5**

6.4 Discussions

6.4.1 Reference point selection

In our approach, we select the reference white as 80 nits based on the sRGB specification and the content metadata, and it is also plausible to map reference white to 100 nits based on the Rec. 709 standard [69]. However, we would also like to ask ourselves: "what will happen if we select reference white at higher luminance?" To answer this question, we did a comparison assuming that the peak brightness of the SDR display is 400 nits, the results are show in Figure 44. Figure 44 (a) is the simulated HDR gamut mapped image assuming the reference white is 80 nits whereas for Figure 44 (b) the reference white is 300 nits. We can clearly tell that when we increase luminance of the reference white, the overall image brightness is enhanced. However, we lose local contrast in the highlight region. This is predictable as we have less luminance range to compress the highlights. The extreme case has already been shown in Figure 4 where reference white equals display white and all the highlights are clipped. In fact, if we look at ST-2084 standard we can tell that the intention of HDR display is not to have contents with higher overall image brightness, but to have more room faithfully reproducing the highlights. Because of this intention, the average pixel level (APL) of an HDR display should be similar to an SDR display and the reference white should also be similar to contemporary TVs, which is around 100 nits. In this sense, mapping reference white to luminance range larger than 100 nits might violate the content creators' intention.

Figure 44: HDR gamut mapped versions of Figure 42 (5) with reference white of (a) 80 nits and (b) 300 nits.

6.4.2 Color spaces for HDR processing,

When we talk about gamut mapping, we need to define in which color space the mapping will take place. In our experiment, we have used an extend-IPT color space because of its hue linearity. At the same time, it is possible to use a color space based on a color appearance model (CAM) to do the gamut mapping, as illustrated in Figure 45. This image is a HDR gamut mapped version of Figure 42 (2) using a modified version of CIECAM02 [122, 123] and it is clear this image looks quite pleasing visually. The reasons we did not use CIECAM02 at first sight were twofold: 1. CIECAM02 has the "yellow-blue" and "purple" problems [124], and currently there is no universally agreed approach to avoid these problems; 2. CIECAM02 is not intended for high luminance level and highly saturate colors. And there are actually limited visual data [26, 112] concerning highly saturate colors and high luminance level. Still doing HDR gamut mapping using a color appearance model could be an interesting next step. In my opinion, a color appearance model tested and intended for both high luminance levels and highly saturated colors can definitely benefit the whole industry.

Figure 45: HDR gamut mapping using a modified version of CIECAM02.

6.5 Summary

In summary, with our proposed HDR gamut mapping approach, it is possible to faithfully reproduce HDR content on SDR display. At the same time, this approach can be incorporated into low level hardware as a 3D LUT. The algorithm is validated through hardware implementation and psychophysical experiment. The psychophysical experiment also indicates that with luminance range between 0.1 to 640 nits, it is possible to make the SDR display resemble an HDR display.

CHAPTER SEVEN: CONCLUSION

High dynamic range is a key parameter for display systems. In this dissertation, we attack the dynamic range problems for two display systems: AR system and HDR displays.

For the AR system, we focuses on three areas: higher ACR, more compact system and broader usage. We achieved these three goals simultaneously by combing a smart dimmer with a functional reflective polarizer. The smart dimmer is a dye-doped LC film that can be electrically tuned for different transmittance. With a tunable transmittance range between 73%~26%, the smart dimmer has one of the best performances on the market. At the same time, the smart dimmer is at least 10X faster than conventional transition glasses. The functional reflective polarizer works similarly to a PBS, except that it is much more lightweight and compact. At the same time, by carefully designing the transmittance spectra of the functional reflective polarizer, the device can help those people with CVD by improving the content contrast and color saturation. Thus making AR system no longer a privilege for people with normal vision.

As for HDR display, we improved its performances both from the hardware side and from the firmware/software side. From the hardware side, we solved the three main challenges of HDR display: contrast ratio (luminance range), color gamut and bit depth.

To solve the problem of contrast ratio, we proposed the dual LCD panel approach. Our analysis indicates that with the dual panel approach, it is possible to achieve high contrast ratio and wide viewing angle simultaneously. The potential thickness and alignment problems of this approach is also discussed. Moreover, to mitigate the Moiré effect, we proposed the PDSF approach. The experiments confirm its effectiveness.

HDR display also comes with a wider color gamut: the Rec. 2020 color gamut. We demonstrated that QDs could be a good candidate to achieve such a wide color gamut. Both PL and EL QDs have been extensively studied and we analyzed the trade-off between optical efficiency and color gamut. Our analysis indicates that with proper QD spectra tuning and color filter optimization, both PL and EL QDs are able to achieve over 90% of the Rec. 2020 color gamut. The color shift of both QD-LCD and QLED is discussed. At the same time, we compare the QDs with the popular 2p-LED approach. Our results illustrated that QDs are still superior to 2p-LEDs because of its design flexibility and highly saturated green colors.

In terms of bit-depth, HDR comes with the PQ encoding to accompany the enlarged luminance range. The 12-bit PQ curve covering 0-10000 nits is regarded as an ultimate goal for the display industry. For local dimming based HDR display, our experimental results indicate that driving the backlight or LC individually is not practical because of its sluggish response time. To achieve the 12-bit PQ curve, we have to drive the backlight and LC simultaneously. Based on this general idea, we proposed a driving scheme that can mitigate the problem of imaging noises. With this driving scheme, the response speed of LC is no longer a problem for HDR displays.

From the firmware/software side, we demonstrated that by mapping reference white to display white, contemporary display pipelines could not reproduce HDR contents correctly. We proposed an improvement to the display pipelines by gamut mapping the HDR contents. With this color-by-color approach, we can display HDR contents adaptively based on the display specifications, even for SDR displays. At the same time, this color-by-color reproduction scheme does not consume much computing power. To test the effectiveness of our scheme, we built up an HDR display and conducted a psychophysical experiment by image comparison. Our experimental results indicate the black level and peak brightness of the display have to be improved

simultaneously. Moreover, to make a display HDR-like, the minimum requirements for luminance range should be between 0.1-640 nits. These results can help future HDR display designs.

APPENDIX: STUDENT PUBLICATIONS

Patents

1. Y.-S. Tsai, K.-C. Lee, S.-T. Wu, G. Tan and R. Zhu, "**DISPLAY DEVICE AND OPTICAL FILM**". US Patent 9,680,132 B1 (June 2017).

JOURNAL PUBLICATIONS

1. **R. Zhu**, H. Chen, and S. T. Wu, "**Achieving 12-bit perceptual quantizer curve with liquid crystal display**," Opt. Express 25(10), 10939-10946 (2017).
2. H. Chen, **R. Zhu**, J. He, W. Duan, W. Hu, Y.Q. Lu, M. C. Li, S. L. Lee, Y. Dong, and S. T. Wu, "**Going beyond the limit of an LCD's color gamut**," Light: Science and Applications 6, e17043 (2017).
3. H. Chen, **R. Zhu**, M. C. Li, S. L. Lee, and S. T. Wu, "**Pixel-by-pixel local dimming for high-dynamic-range liquid crystal displays**," Opt. Express 25(3), 1973-1984 (2017).
4. H. Chen, **R. Zhu**, G. Tan, M.C. Li, S.-L. Lee, and S. T. Wu, "**Enlarging the color gamut of liquid crystal displays with a functional reflective polarizer**," Opt. Express 25(1), 102-111 (2017).
5. **R. Zhu**, G. Tan, J. Yuan and S.-T. Wu, "**Functional reflective polarizer for augmented reality and color vision deficiency**", Opt. Express 24(5), 5431-5441 (2016).
6. Y. Wang, J. He, H. Chen, J. Chen, **R. Zhu,** P. Ma, A. Towers, Y. Lin, A. J. Gesquiere, S.-T. Wu, Y. Dong, "**Ultrastable, Highly Luminescent Organic-Inorganic Perovskite-Polymer Composite Films**", Adv. Mater. 28(48), 10710-10717 (2016).
7. G. Tan, **R. Zhu**, Y. S. Tsai, K. C. Lee, Z. Luo, Y. Z. Lee, and S. T. Wu, "**High ambient contrast ratio OLED and QLED without a circular polarizer**," J. Phys. D: Appl. Phys. 49, 315101 (2016).

8. H. Chen, **R. Zhu**, Y. H. Lee, and S. T. Wu, "**Correlated color temperature tunable white LED with a dynamic color filter**," Opt. Express 24(6), A731-A739 (2016).

9. ***(JSID Outstanding Student Paper of the Year)*** **R. Zhu**, H. Chen, T. Kosa, P. Coutino, G. Tan and S.-T. Wu, "**High-ambient-contrast augmented reality with a tunable transmittance liquid crystal film and a functional reflective polarizer**", J. SID 24(4), 229-233 (2016).

10. H. Liang, Z. Luo, **R. Zhu**, Y. Dong, J.-H. Lee, J. Zhou and S.-T. Wu, "**High efficiency quantum dot and organic LEDs with a back-cavity and a high index substrate**," J. Phys. D: Appl. Phys. 49(14), 145103 (2016).

11. **R. Zhu**, Q. Hong, H. Zhang, and S. T. Wu, "**Freeform reflector for architectural lighting**", Opt. Express 23(25), 31828-31837 (2015).

12. Z. Luo, G. Zhang, **R. Zhu**, Y. Gao, and S. T. Wu, "**Polarizing grating color filters with large acceptance angle and high transmittance**", Appl. Opt. 55(1), 70-76 (Jan. 2016).

13. **R. Zhu**, Z. Luo, H. Chen, Y. Dong, and S.T. Wu, "**Realizing Rec. 2020 color gamut with quantum dot displays**," Opt. Express 23(18), 23680-23693 (2015).

14. H. Chen, **R. Zhu**, J. Zhu, and S.T. Wu, "**A simple method to measure the twist elastic constant of a nematic liquid crystal**," Liq. Cryst. 42, 1738-1742 (Dec. 2015)

15. **R. Zhu**, Q. Hong, Y. Gao, Z. Luo, S.T. Wu, M.C. Li, S.L. Lee, and W.C. Tsai, "**Tailoring the light distribution of liquid crystal display with freeform engineered diffuser**," Opt. Express 23(11), 14070-14084 (2015).

16. H. Liang, **R. Zhu**, Y. Dong, S. T. Wu, J. Li, J. Wang, and J. Zhou, "**Enhancing the outcoupling efficiency of quantum dot LEDs with internal nano-scattering pattern**," Opt. Express 23(10), 12910-12922 (2015).

17. H. Chen, Z. Luo, **R. Zhu**, Q. Hong, and S. T. Wu, "**Tuning the correlated color temperature of white LED with a guest-host liquid crystal**," Opt. Express 23(10), 13060-13068 (2015).

18. (***Invited paper***) Y. Gao, Z. Luo, **R. Zhu**, Q. Hong, S. T. Wu, M. C. Li, S. L. Lee, and W. C. Tsai, "**A high performance single-domain LCD with wide luminance distribution,"** J. Display Technology **11**(4), 315-324 (2015).

19. **R. Zhu**, Z. Luo, and S.T. Wu, "**Light extraction analysis and improvement in a quantum dot light emitting diode**," Opt. Express **22**(S7), A1783-A1798 (2014).

20. **R. Zhu**, S. Xu, Q. Hong, S.T. Wu, C. Lee, C. M. Yang, C. C. Lo, and A. Lien, "**A polymeric lens embedded 2D/3D switchable display with dramatically reduced crosstalk**," Appl. Opt. **53**(7), 1388-1395 (2014).

21. Y. Liu, Y. F. Lan, H. Zhang, **R. Zhu**, D. Xu, C.Y. Tsai, J.K. Lu, N. Sugiura, Y.C. Lin and S.T. Wu, "**Optical rotatory power of polymer-stabilized blue phase liquid crystals**," Appl. Phys. Lett. **102**, 131102 (2013).

22. Y. Zhang, X. Zhang, Y. Wang, **R. Zhu**, Y. Gai, X. Liu, and P. Yuan, "**Reversible Fano resonance by transition from fast light to slow light in a coupled-resonator induced transparency structure,**" Opt. Express **21**(7), 8570-8586 (2013)

23. X. Zhang, Y. Zhang, H. Tian, H. Wu, G. Li, **R. Zhu** and P. Yuan, "**Ultrahigh sensitivity of rotation sensing beyond the tradeoff between sensitivity and linewidth by the storage of light in a dynamic slow-light resonator**," Phys. Rev. A 84, 063823 (2011).

CONFERENCE PROCEEDINGS

1. **R. Zhu**, A. Sarkar, N. Emerton and T. Large, "**Reproducing High-Dynamic-Range Contents Adaptively Based on Display Specifications**", SID. Symp. Digest 2017, Los Angeles, CA.
2. H. Chen, **R. Zhu**, M.-C. Li, S.-L. Lee, and S. T. Wu, "**High Dynamic Range LCD with Pixel-level Local Dimming**," SID. Symp. Digest 2017, Los Angeles, CA.
3. H. Chen, **R. Zhu**, G. Tan, M.-C. Li, S.-L. Lee, and S. T. Wu, "**Wide-Color-Gamut LCD with a Functional Reflective Polarizer**," SID. Symp. Digest 2017, Los Angeles, CA.
4. J. He, H. Chen, H. Chen, Y. Wang, J. Chen, **R. Zhu**, S. T. Wu, and Y. Dong, "Wide color gamut LCDs with narrow green emitting films," Proc. SPIE 10125, 101251D (2017).
5. (***SID distinguished student paper***) **R. Zhu**, H. Chen, T. Kosa, P. Coutino, G. Tan and S.T. Wu, "**A High-Ambient-Contrast Augmented-Reality System**", SID Symp. Digest 2016, San Francisco, CA.
6. **R. Zhu**, Z. Luo, H. Chen, Y. Dong and S.T. Wu, "**Quantum-Dot LCDs for Rec. 2020**", SID Symp. Digest 2016, San Francisco, CA.
7. **R. Zhu**, Q. Hong, H. Zhang and S.T. Wu, "**Effective Architectural Lighting with Free-Form Optics**", SID Symp. Digest 2016, San Francisco, CA.
8. G. Tan, **R. Zhu**, Y.S. Tsai, K.C. Lee, Z. Luo, Y.Z Lee and S.T. Wu, "**High-Ambient Contrast-Ratio OLED and Quantum-Dot LED without a Circular Polarizer**", SID Symp. Digest 2016, San Francisco, CA.
9. H. Chen, **R. Zhu**, K. Käläntär and S.T. Wu, "**Quantum-Dot-Enhanced LCDs with Wide Color Gamut and Broad Angular Luminance Distribution**", SID Symp. Digest 2016, San Francisco, CA.

10. H. Chen, **R. Zhu**, Y.H. Lee and S.T. Wu, "**Correlated-Color-Temperature Tunable WLED for Smart Lighting**", SID Symp. Digest 2016, San Francisco, CA.

11. Z. Luo, G. Zhang, Y. Gao, **R. Zhu** and S.T. Wu, "**Tripling LCD-BLU Efficiency by Simultaneous Color and Polarization Recycling**", SID Symp. Digest 2016, San Francisco, CA.

12. **R. Zhu**, Z. Luo and S.T. Wu. "**Doubling the Light Outcoupling Efficiency of Quantum Dot Light Emitting Diodes**," SID Symp. Digest 2015, San Jose, CA.

13. (***SID Distinguished Student Poster***) Y. Gao, Z. Luo, **R. Zhu**, Q. Hong, S. T. Wu, M.-C. Li, S.-L. Lee, and W.-C. Tsai. "**An LCD with OLED-like Luminance Distribution**," SID Symp. Digest 2015, San Jose, CA.

14. H. Liang, **R. Zhu**, S.T. Wu, J. Li, J. Wang, and J. Zhou. "**Enhancing the Light Outcoupling Efficiency of Quantum-Dot Light Emitting Diodes with Periodic Microstructures**," SID Symp. Digest 2015, San Jose, CA.

15. **R. Zhu**, S. Xu, Q. Hong, S.T. Wu, C. Lee, C. M. Yang, C. C. Lo, and A. Lien, "**A polymeric lens embedded 2D/3D switchable display with dramatically reduced crosstalk**," SID Symposium Digest 2014, San Diego, CA.

16. Y. Liu, H. Zhang, **R. Zhu**, D. Xu, S. T. Wu, Y. F. Lan, C. Y. Tsai, J. K. Lu, N. Sugiura and Y. C. Lin, "**Enhancing the contrast ratio of blue phase LCDs**," SID Symposium Digest 2013, Vancouver, Canada.

REFERENCES

1. H. Seetzen, W. Heidrich, W. Stuerzlinger, G. Ward, L. Whitehead, M. Trentacoste, A. Ghosh, and A. Vorozcovs, "High dynamic range display systems," ACM Trans. Graph. **23**(3), 760-768 (2004).
2. M. D. Fairchild, "The HDR photographic survey," in *IS&T/SID 15th Color Imaging Conference*, (2007), 233-238.
3. M. D. Fairchild, "Seeing, adapting to, and reproducing the appearance of nature," Appl. Opt. **54**(4), B107-B116 (2015).
4. J. P. Rolland and H. Fuchs, "Optical Versus Video See-Through Head-Mounted Displays in Medical Visualization," Presence-Teleop. Virt. **9**(3), 287-309 (2000).
5. J. K. Yoon, E. M. Park, J. S. Son, H. W. Shin, H. E. Kim, M. Yee, H. G. Kim, C. H. Oh, and B. C. Ahn, "The study of picture quality of OLED TV with WRGB OLEDs structure," SID Symp. Dig. Tech. Pap. **44**(1), 326-329 (2013).
6. A. Olwal, C. Lindfors, J. Gustafsson, T. Kjellberg, and L. Mattsson, "ASTOR: An Autostereoscopic Optical See-through Augmented Reality System," in *Proceedings of the 4th IEEE/ACM International Symposium on Mixed and Augmented Reality*, (2005), 24-27.
7. S. Lee, X. Hu, and H. Hua, "Effects of Optical Combiner and IPD Change for Convergence on Near-Field Depth Perception in an Optical See-Through HMD," IEEE Trans. Vis. Comput. Graphics **PP**(99), 1-1 (2015).
8. F. Zhou, H. B.-L. Duh, and M. Billinghurst, "Trends in augmented reality tracking, interaction and display: A review of ten years of ISMAR," in *Proceedings of the 7th IEEE/ACM International Symposium on Mixed and Augmented Reality*, (2008), 193-202.

9. X. Hu and H. Hua, "High-resolution optical see-through multi-focal-plane head-mounted display using freeform optics," Opt. Express **22**(11), 13896-13903 (2014).

10. R. Zhang and H. Hua, "Characterizing polarization management in a p-HMPD system," Appl. Opt. **47**(4), 512-522 (2008).

11. R. Zhu, G. Tan, J. Yuan, and S.-T. Wu, "Functional reflective polarizer for augmented reality and color vision deficiency," Opt. Express **24**(5), 5431-5441 (2016).

12. Y. Li, T. X. Wu, and S.-T. Wu, "Design Optimization of Reflective Polarizers for LCD Backlight Recycling," J. Display Technol. **5**(8), 335-340 (2009).

13. M. F. Weber, C. A. Stover, L. R. Gilbert, T. J. Nevitt, and A. J. Ouderkirk, "Giant Birefringent Optics in Multilayer Polymer Mirrors," Science **287**(5462), 2451-2456 (2000).

14. M. Alpern and T. Wake, "Cone pigments in human deutan colour vision defects," J. Physiol. **266**(3), 595-612 (1977).

15. M. Neitz and J. Neitz, "Molecular genetics of color vision and color vision defects," Arch. Ophthalmol. **118**(5), 691-700 (2000).

16. J. Kuang, G. M. Johnson, and M. D. Fairchild, "iCAM06: A refined image appearance model for HDR image rendering," J Vis. Commun. Image Represent. **18**(5), 406-414 (2007).

17. M. D. Fairchild, *Color Apperance Models*, 3rd ed. (Wiley, 2013).

18. S. Daly, T. Kunkel, X. Sun, S. Farrell, and P. Crum, "41.1: Distinguished Paper: Viewer Preferences for Shadow, Diffuse, Specular, and Emissive Luminance Limits of High Dynamic Range Displays," SID Symp. Dig. Tech. Pap. **44**(1), 563-566 (2013).

19. D. M. Hoffman, N. N. Stepien, and W. Xiong, "The importance of native panel contrast and local dimming density on perceived image quality of high dynamic range displays," J. Soc. Info. Display **24**(4), 216-228 (2016).

20. E. Reinhard, W. Heidrich, P. Debevec, S. Pattanaik, G. Ward, and M. Karol, *High Dynamic Range Imaging, Second Edition: Acquisition, Display, and Image-Based Lighting*, 2nd ed. (Morgan Kaufmann, 2010).

21. E. Reinhard, T. Kunkel, Y. Marion, J. Brouillat, R. Cozot, and K. Bouatouch, "Image display algorithms for high- and low-dynamic-range display devices," J. Soc. Info. Display **15**(12), 997-1014 (2007).

22. H. Chen, R. Zhu, M.-C. Li, S.-L. Lee, and S.-T. Wu, "Pixel-by-pixel local dimming for high-dynamic-range liquid crystal displays," Opt. Express **25**(3), 1973-1984 (2017).

23. ITU-R Recommendation BT.2020 "Parameter values for ultra-high definition television systems for production and international programme exchange," (2012).

24. K. Masaoka and Y. Nishida, "Metric of color-space coverage for wide-gamut displays," Opt. Express **23**(6), 7802-7808 (2015).

25. R. Zhu, Z. Luo, H. Chen, Y. Dong, and S.-T. Wu, "Realizing Rec. 2020 color gamut with quantum dot displays," Opt. Express **23**(18), 23680-23693 (2015).

26. K. Masaoka, Y. Kusakabe, T. Yamashita, Y. Nishida, T. Ikeda, and M. Sugawara, "Algorithm Design for Gamut Mapping From UHDTV to HDTV," J. Display Technol. **12**(7), 760-769 (2016).

27. J. Morovič, *Color Gamut Mapping* (Wiley, 2008).

28. R. Zhu, A. Sarkar, N. Emerton, and T. Large, "81-3: Reproducing High Dynamic Range Contents Adaptively based on Display Specifications," SID Symp. Dig. Tech. Pap. **48**(1), 1188-1191 (2017).

29. R. W. Floyd and L. Steinberg, "Adaptive algorithm for spatial greyscale," SID Symp. Dig. Tech. Pap. **17**75-77 (1976).

30. SMPTE ST-2084, "High Dynamic Range Electro-Optical Transfer Function of Mastering Reference Displays," (2014).

31. R. Zhu, Z. Luo, and S.-T. Wu, "Light extraction analysis and enhancement in a quantum dot light emitting diode," Opt. Express **22**(S7), A1783-A1798 (2014).

32. S. T. Wu and C. S. Wu, "Mixed‐mode twisted nematic liquid crystal cells for reflective displays," Appl. Phys. Lett. **68**(11), 1455-1457 (1996).

33. H. De Smet, D. Cuypers, A. Van Calster, J. Van den Steen, and G. Van Doorselaer, "Design, fabrication and evaluation of a high-performance XGA VAN-LCOS microdisplay," Displays **23**(3), 89-98 (2002).

34. S. He, J.-H. Lee, H.-C. Cheng, J. Yan, and S.-T. Wu, "Fast-Response Blue-Phase Liquid Crystal for Color-Sequential Projection Displays," J. Display Technol. **8**(6), 352-356 (2012).

35. H. Brettel, F. Viénot, and J. D. Mollon, "Computerized simulation of color appearance for dichromats," J. Opt. Soc. Am. A **14**(10), 2647-2655 (1997).

36. G. M. Machado, M. M. Oliveira, and L. A. F. Fernandes, "A Physiologically-based Model for Simulation of Color Vision Deficiency," IEEE Trans. Vis. Comput. Graphics **15**(6), 1291-1298 (2009).

37. G. Wirnsberger, B. J. Scott, B. F. Chmelka, and G. D. Stucky, "Fast Response Photochromic Mesostructures," Adv. Mater. **12**(19), 1450-1454 (2000).

38. J. G. Milton and A. Longtin, "Evaluation of pupil constriction and dilation from cycling measurements," Vis. Res. **30**(4), 515-525 (1990).

39. B. Bahadur, *Liquid Crystals: Applications and Uses* (World Science Publishing Co., Singapore, 1991).

40. S.-T. Wu, C.-S. Wu, and K.-W. Lin, "Chiral-homeotropic liquid crystal cells for high contrast and low voltage displays," J. Appl. Phys. **82**(10), 4795-4799 (1997).

41. T. Alfrey, E. F. Gurnee, and W. J. Schrenk, "Physical optics of iridescent multilayered plastic films," Polym. Eng. Sci. **9**(6), 400-404 (1969).

42. D. W. Berreman, "Optics in Stratified and Anisotropic Media: 4×4-Matrix Formulation," J. Opt. Soc. Am. **62**(4), 502-510 (1972).

43. Y. Huang, T. X. Wu, and S.-T. Wu, "Simulations of liquid-crystal Fabry–Perot etalons by an improved 4×4 matrix method," J. Appl. Phys. **93**(5), 2490-2495 (2003).

44. P. Yeh, *Optical Waves in Layered Media* (Wiley, 1988).

45. J. Li, G. Baird, Y.-H. Lin, H. Ren, and S.-T. Wu, "Refractive-index matching between liquid crystals and photopolymers," J. Soc. Info. Display **13**(12), 1017-1026 (2005).

46. T. Higashihara and M. Ueda, "Recent Progress in High Refractive Index Polymers," Macromolecules **48**(7), 1915-1929 (2015).

47. D. H. Brainard, H. Jiang, N. P. Cottaris, F. Rieke, E. J. Chichilnisky, J. E. Farrell, and B. A. Wandell, "ISETBIO: Computational tools for modeling early human vision," in *Imaging and Applied Optics 2015*, OSA Technical Digest (online) (2015), IT4A.4.

48. C.-H. Oh, H.-J. Shin, W.-J. Nam, B.-C. Ahn, S.-Y. Cha, and S.-D. Yeo, "Technological progress and commercialization of OLED TV," SID Symp. Dig. Tech. Pap. **44**(1), 239-242 (2013).

49. H. Chen, T. H. Ha, J. H. Sung, H. R. Kim, and B. H. Han, "Evaluation of LCD local-dimming-backlight system," J. Soc. Info. Display **18**(1), 57-65 (2010).

50. F.-C. Lin, Y.-P. Huang, L.-Y. Liao, C.-Y. Liao, H.-P. D. Shieh, T.-M. Wang, and S.-C. Yeh, "Dynamic Backlight Gamma on High Dynamic Range LCD TVs," J. Display Technol. **4**(2), 139-146 (2008).

51. K. J. Kwon, M. B. Kim, C. Heo, S. G. Kim, J. S. Baek, and Y. H. Kim, "Wide color gamut and high dynamic range displays using RGBW LCDs," Displays **40**9-16 (2015).

52. D. Lanman, M. Hirsch, Y. Kim, and R. Raskar, "Content-adaptive parallax barriers: optimizing dual-layer 3D displays using low-rank light field factorization," ACM Trans. Graph. **29**(6), 1-10 (2010).

53. D. Lanman, G. Wetzstein, M. Hirsch, W. Heidrich, and R. Raskar, "Polarization fields: dynamic light field display using multi-layer LCDs," ACM Trans. Graph. **30**(6), 1-10 (2011).

54. F.-C. Huang, K. Chen, and G. Wetzstein, "The light field stereoscope: immersive computer graphics via factored near-eye light field displays with focus cues," ACM Trans. Graph. **34**(4), 1-12 (2015).

55. M. Schadt and W. Helfrich, "VOLTAGE - DEPENDENT OPTICAL ACTIVITY OF A TWISTED NEMATIC LIQUID CRYSTAL," Appl. Phys. Lett. **18**(4), 127-128 (1971).

56. A. Takeda, S. Kataoka, T. Sasaki, H. Chida, H. Tsuda, K. Ohmuro, T. Sasabayashi, Y. Koike, and K. Okamoto, "41.1: A Super-High Image Quality Multi-Domain Vertical

Alignment LCD by New Rubbing-Less Technology," SID Symp. Dig. Tech. Pap. **29**(1), 1077-1080 (1998).

57. S. H. Lee, S. L. Lee, and H. Y. Kim, "Electro-optic characteristics and switching principle of a nematic liquid crystal cell controlled by fringe-field switching," Appl. Phys. Lett. **73**(20), 2881-2883 (1998).

58. H. Chen, F. Peng, Z. Luo, D. Xu, S.-T. Wu, M.-C. Li, S.-L. Lee, and W.-C. Tsai, "High performance liquid crystal displays with a low dielectric constant material," Opt. Mater. Express **4**(11), 2262-2273 (2014).

59. H. Chen, R. Zhu, J. Zhu, and S.-T. Wu, "A simple method to measure the twist elastic constant of a nematic liquid crystal," Liq. Cryst. **42**(12), 1738-1742 (2015).

60. A. Chao, K. T. Huang, C. W. Tsai, Y. W. Hung, H. F. Cheng, W. Yeh, C. H. Yu, and H. H. Wu, "P-107: The Fastest Response TN-Type TFT LCD of the World Likes OCB Level," SID Symp. Dig. Tech. Pap. **38**(1), 603-606 (2007).

61. H. Chen, Z. Luo, D. Xu, F. Peng, S.-T. Wu, M.-C. Li, S.-L. Lee, and W.-C. Tsai, "43.4: Distinguished Student Paper: A Fast-Response A-Film-Enhanced Fringe Field Switching LCD," SID Symp. Dig. Tech. Pap. **46**(1), 656-660 (2015).

62. H. Chen, M. Hu, F. Peng, J. Li, Z. An, and S.-T. Wu, "Ultra-low viscosity liquid crystal materials," Opt. Mater. Express **5**(3), 655-660 (2015).

63. F. Peng, H. Chen, F. Gou, Y.-H. Lee, M. Wand, M.-C. Li, S.-L. Lee, and S.-T. Wu, "Analytical equation for the motion picture response time of display devices," J. Appl. Phys. **121**(2), 023108 (2017).

64. H. Chen, F. Peng, F. Gou, Y.-H. Lee, M. Wand, and S.-T. Wu, "Nematic LCD with motion picture response time comparable to organic LEDs," Optica **3**(9), 1033-1034 (2016).

65. G. Guarnieri, L. Albani, and G. Ramponi, "Minimum-Error Splitting Algorithm for a Dual Layer LCD Display—Part I: Background and Theory," J. Display Technol. **4**(4), 383-390 (2008).

66. G. Guarnieri, L. Albani, and G. Ramponi, "Minimum-Error Splitting Algorithm for a Dual Layer LCD Display—Part II: Implementation and Results," J. Display Technol. **4**(4), 391-397 (2008).

67. A. Moheghi, H. Nemati, and D.-K. Yang, "Polarizing light waveguide plate from polymer stabilized liquid crystals," Opt. Mater. Express **5**(5), 1217-1223 (2015).

68. A. Moheghi, G. Qin, and D.-K. Yang, "Stable polarizing light waveguide plate for edgelit liquid crystal displays," Opt. Mater. Express **6**(2), 429-435 (2016).

69. ITU-R Recommendation BT.709-5, "Parameter values for the HDTV standards for production and international program exchange," (2015).

70. SMPTE RP 431-2, “D-cinema quality — reference projector and environment,” 2011.

71. Adobe Systems Inc., “Adobe RGB (1998) color image encoding,” 2005.

72. K. Masaoka, Y. Nishida, M. Sugawara, and E. Nakasu, "Design of Primaries for a Wide-Gamut Television Colorimetry," IEEE Trans. Broadcast **56**(4), 452-457 (2010).

73. M. R. Pointer, "The Gamut of Real Surface Colours," Color Res. Appl **5**(3), 145-155 (1980).

74. K. Masaoka, Y. Nishida, and M. Sugawara, "Designing display primaries with currently available light sources for UHDTV wide-gamut system colorimetry," Opt. Express **22**(16), 19069-19077 (2014).

75. K. V. Chellappan, E. Erden, and H. Urey, "Laser-based displays: a review," Appl. Opt. **49**(25), F79-F98 (2010).

76. S. Kim, S. H. Im, and S.-W. Kim, "Performance of light-emitting-diode based on quantum dots," Nanoscale **5**(12), 5205-5214 (2013).

77. Z. Luo, Y. Chen, and S.-T. Wu, "Wide color gamut LCD with a quantum dot backlight," Opt. Express **21**(22), 26269 (2013).

78. Z. Luo, D. Xu, and S.-T. Wu, "Emerging quantum-dots-enhanced LCDs," J. Display Technol. **10**(7), 526-539 (2014).

79. X. Dai, Z. Zhang, Y. Jin, Y. Niu, H. Cao, X. Liang, L. Chen, J. Wang, and X. Peng, "Solution-processed, high-performance light-emitting diodes based on quantum dots," Nature **515**(7525), 96-99 (2014).

80. Y. Dong, J.-M. Caruge, Z. Zhou, C. Hamilton, Z. Popovic, J. Ho, M. Stevenson, G. Liu, V. Bulovic, M. Bawendi, P. T. Kazlas, J. Steckel, and S. Coe-Sullivan, "Ultra-Bright, Highly Efficient, Low Roll-off Inverted Quantum-Dot Light Emitting Devices (QLEDs)," SID Symp. Dig. Tech. Pap. **46**(1), 270-273 (2015).

81. H. Shen, W. Cao, N. T. Shewmon, C. Yang, L. S. Li, and J. Xue, "High-Efficiency, Low Turn-on Voltage Blue-Violet Quantum-Dot-Based Light-Emitting Diodes," Nano Lett **15**(2), 1211-1216 (2015).

82. Y. Yang, Y. Zheng, W. Cao, A. Titov, J. Hyvonen, R. MandersJesse, J. Xue, P. H. Holloway, and L. Qian, "High-efficiency light-emitting devices based on quantum dots with tailored nanostructures," Nat. Photonics **9**(4), 259-266 (2015).

83. S. Quan, N. Ohta, R. S. Berns, X. Jiang, and N. Katoh, "Unified Measure of Goodness and Optimal Design of Spectral," J Imaging Sci Technol **46**(6), 485-497 (2002).

84. M. Reyes-Sierra and C. A. C. Coello, "Multi-Objective particle swarm optimizers: a survey of the state-of-the-art," Int. J. Comput. Intell. Res. **2**287-308 (2006).

85. J. S. Steckel, J. Ho, C. Hamilton, C. Breen, W. Liu, P. Allen, J. Xi, and S. Coe-Sullivan, "12.1: Invited Paper: Quantum Dots: The Ultimate Down-Conversion Material for LCD Displays," SID Symp. Dig. Tech. Pap. **45**(1), 130-133 (2014).

86. J. Chen, V. Hardev, J. Hartlove, J. Hofler, and E. Lee, "66.1: Distinguised Paper: A High-Efficiency Wide-Color-Gamut Solid-State Backlight System for LCDs Using Quantum Dot Enhancement Film," SID Symp. Dig. Tech. Pap. **43**(1), 895-896 (2012).

87. M. Schadt, "Milestone in the History of Field-Effect Liquid Crystal Displays and Materials," Jpn. J. Appl. Phys. **48**(3S2), 03B001 (2009).

88. C. A. C. Coello and G. B. Lamont, *Applications of Multi-Objective Evolutionary Algorithms* (World Scientific, 2004).

89. J. S. Steckel, R. Colby, W. Liu, K. Hutchinson, C. Breen, J. Ritter, and S. Coe-Sullivan, "68.1: Invited Paper: Quantum Dot Manufacturing Requirements for the High Volume LCD Market," SID Symp. Dig. Tech. Pap. **44**(1), 943-945 (2013).

90. J.-J. Lyu, J. Sohn, H. Y. Kim, and S. Lee, "Recent Trends on Patterned Vertical Alignment (PVA) and Fringe-Field Switching (FFS) Liquid Crystal Displays for Liquid Crystal Television Applications," J. Display Technol. **3**(4), 404-412 (2007).

91. H. Chen, Z. Luo, D. Xu, F. Peng, S.-T. Wu, M.-C. Li, S.-L. Lee, and W.-C. Tsai, "A fast-response A-film-enhanced fringe field switching liquid crystal display," Liq. Cryst. **42**(4), 537-542 (2015).

92. H. Zhan, Z. Xu, C. Tian, Y. Wang, M. Chen, W. Kim, Z. Bu, X. Shao, and S. Lee, "Achieving standard wide color gamut by tuning LED backlight and color filter spectrum in LCD," J. Soc. Info. Display **22**(11), 545-551 (2014).

93. J. Chen, S. Gensler, J. Hartlove, J. Yurek, E. Lee, J. Thielen, J. Van Derlofske, J. Hillis, G. Benoit, J. Tibbit, and A. Lathrop, "Quantum Dots: Optimizing LCD Systems to Achieve Rec. 2020 Color Performance," SID Symp. Dig. Tech. Pap. **46**(1), 173-175 (2015).

94. J. M. Hillis, J. Thielen, J. Tibbits, A. Lathrop, D. Lamb, and J. Van Derlofske, "Closing in on Rec. 2020 – how close is close enough?," SID Symp. Dig. Tech. Pap. **46**(1), 223-226 (2015).

95. K. Masaoka, Y. Nishida, and M. Sugawara, "Designing display primaries with currently available light sources for UHDTV wide-gamut system colorimetry," Opt. Express **22**(16), 19069-19077 (2014).

96. K. A. Neyts, "Simulation of light emission from thin-film microcavities," J. Opt. Soc. Am. A **15**(4), 962-971 (1998).

97. H. Liang, R. Zhu, Y. Dong, S.-T. Wu, J. Li, J. Wang, and J. Zhou, "Enhancing the outcoupling efficiency of quantum dot LEDs with internal nano-scattering pattern," Opt. Express **23**(10), 12910-12922 (2015).

98. M. D. Fairchild and R. L. Heckaman, "Measuring observer metamerism: The Nimeroff approach," Color Res. Appl **41**(2), 115-124 (2016).

99. A. Sarkar, F. Autrusseau, F. Viénot, P. Le Callet, and L. Blondé, "From CIE 2006 physiological model to improved age-dependent and average colorimetric observers," J. Opt. Soc. Am. A **28**(10), 2033-2048 (2011).

100. R. Lu, Q. Hong, Z. Ge, and S.-T. Wu, "Color shift reduction of a multi-domain IPS-LCD using RGB-LED backlight," Opt. Express **14**(13), 6243-6252 (2006).

101. S.-S. Park, I. Sohn, E. Cho, S. Park, and E. Kim, "Color Shift Reduction of Liquid Crystal Displays by Controlling Light Distribution Using a Micro-Lens Array Film," J. Display Technol. **8**(11), 643-649 (2012).

102. S. Hofmann, M. Thomschke, P. Freitag, M. Furno, B. Lüssem, and K. Leo, "Top-emitting organic light-emitting diodes: Influence of cavity design," Appl. Phys. Lett. **97**(25), 253308 (2010).

103. Y. Ito, T. Hori, H. Tani, Y. Ueno, T. Kusunoki, H. Nomura, and H. Kondo, "59.1: A Backlight System with a Phosphor Sheet Providing both Wider Color Gamut and Higher Efficiency," SID Symp. Dig. Tech. Pap. **44**(1), 816-819 (2013).

104. P. Li, Z. Wang, Q. Guo, and Z. Yang, "Luminescence and energy transfer of 432 nm blue LED radiation-converting phosphor $Ca_4Y_6O(SiO_4)_6$:Eu^{2+}, Mn^{2+} for warm white LEDs," RSC Advances **5**(6), 4448-4453 (2015).

105. E. Jang, S. Jun, H. Jang, J. Lim, B. Kim, and Y. Kim, "White-Light-Emitting Diodes with Quantum Dot Color Converters for Display Backlights," Adv. Mater. **22**(28), 3076-3080 (2010).

106. J. H. Oh, H. Kang, M. Ko, and Y. R. Do, "Analysis of wide color gamut of green/red bilayered freestanding phosphor film-capped white LEDs for LCD backlight," Opt. Express **23**(15), A791-A804 (2015).

107. T. Kunkel, S. Spears, R. Atkins, T. Pruitt, and S. Daly, "65-1: Invited Paper: Characterizing High Dynamic Range Display System Properties in the Context of Today's Flexible Ecosystems," SID Symp. Dig. Tech. Pap. **47**(1), 880-883 (2016).

108. M. F. Schiekel and K. Fahrenschon, "Deformation of Nematic Liquid Crystals with Vertical Orientation in Electrical Fields," Appl. Phys. Lett. **19**(10), 391-393 (1971).

109. H. Chen, F. Gou, and S.-T. Wu, "Submillisecond-response nematic liquid crystals for augmented reality displays," Opt. Mater. Express **7**(1), 195-201 (2017).

110. S.-T. Wu, "Design of a liquid crystal based tunable electrooptic filter," Appl. Opt. **28**(1), 48-52 (1989).

111. R. H. Chan, H. Chung-Wa, and M. Nikolova, "Salt-and-pepper noise removal by median-type noise detectors and detail-preserving regularization," IEEE Trans. Image Process. **14**(10), 1479-1485 (2005).

112. M. R. Luo, A. A. Clarke, P. A. Rhodes, A. Schappo, S. A. R. Scrivener, and C. J. Tait, "Quantifying colour appearance. Part I. Lutchi colour appearance data," Color Res. Appl **16**(3), 166-180 (1991).

113. K. Käläntär, "A monolithic segmented functional light guide for 2-D dimming LCD backlight," J. Soc. Info. Display **19**(1), 37-47 (2011).

114. E. Reinhard, M. Stark, P. Shirley, and J. Ferwerda, "Photographic tone reproduction for digital images," ACM Trans. Graph. **21**(3), 267-276 (2002).

115. B. Min, H. Wey, and Y. Moon, "Paper No S8.1: Color Volume-Based Wide Color Gamut Mapping for Rec. 2020 Contents in Digital Television," SID Symp. Dig. Tech. Pap. **46**(S1), 33-33 (2015).

116. W. Redmann, P. Andrivon, P. Bordes, and F. Urban, "Reference-Based Color Volume Remapping," in *SMPTE 2015 Annual Technical Conference and Exhibition*, (2015), 1-14.

117. IEC 61966-2-1, "Multimedia systems and equipment-colour measurement and management—part 2-1: Colour management—default rgb colour space—srgb," (1999).

118. F. Ebner and M. D. Fairchild, "Development and Testing of a Color Space (IPT) with Improved Hue Uniformity," in *IS&T 6th Color and Imaging Conference*, (1998), pp. 8-13.

119. CIE. 156:2004, "Guidelines for the evaluation of gamut mapping algorithms," (2004).

120. J. Kuang, R. Heckaman, and M. D. Fairchild, "Evaluation of HDR tone-mapping algorithms using a high-dynamic-range display to emulate real scenes," J. Soc. Info. Display **18**(7), 461-468 (2010).

121. J. Wu, X. Feng, and S. J. Daly, "Sub-pixel-based MVA LCTV characterization and color modeling," in *Proc. SPIE 7241*, (2009), 72410C-72410C-72412.

122. CIE. 159:2004, "A colour appearance model for colour management systems: CIECAM02", (2014).

123. C. Li, Z. Li, Z. Wang, Y. Xu, M. R. Luo, G. Cui, M. Melgosa, and M. R. Pointer, "A Revision of CIECAM02 and its CAT and UCS," in *IS&T 24 Color and Imaging Conference*, (2016).

124. J. Jiang, Z. Wang, M. R. Luo, M. Melgosa, M. H. Brill, and C. Li, "Optimum solution of the CIECAM02 yellow–blue and purple problems," Color Res. Appl **40**(5), 491-503 (2015).